Depth of Sudden Velocity Changes derived from Multi-Mode Rayleigh Waves

Claudia Finger[1] and Katrin Löer[2]

[1]Fraunhofer IEG, Fraunhofer Institute for Energy Infrastructures and Geothermal Systems (IEG)
[2]TU Delft

November 22, 2023

Abstract

To integrate structural subsurface models and smooth seismic velocity models, they need to share common features and resolutions. Here, we propose a new approach for estimating the depth of sudden velocity changes from ambient-noise multi-mode Rayleigh waves applicable to a wide range of frequencies. Approximating the size and shape of the so-called energy ellipse at frequencies where the ellipticity has an extremum allows us to derive the depth of sudden velocity changes as the half height of the energy ellipse. We test our approach theoretically, numerically, and on real data from two geothermal sites by extracting Rayleigh wave ellipticities and phase velocities from three-component beamforming of ambient noise using the python code package B3AMpy. For a small-scale array, our approach validates the depth of quaternary sediments predicted by geological models. For deeper velocity changes, high uncertainties remain but the general trend of inclining boundaries can be recovered well. We demonstrate that, if impedance contrasts are larger than three, our approach is valid for multiple layers, laterally heterogeneous models, and a wide range of Poisson ratios.

Depth of Sudden Velocity Changes derived from Multi-Mode Rayleigh Waves

C. Finger[1] and K. Löer[2]

[1]Fraunhofer IEG, Fraunhofer Institution for Energy Infrastructures and Geothermal Systems
[2]School of Geosciences , University of Aberdeen, now: Department of Geoscience & Engineering TU Delft

Key Points:

- We estimate the depth of sudden velocity increases from phase velocity and ellipticity of ambient-noise multi-mode Rayleigh waves
- Three-component ambient-noise beamforming is used to estimate phase velocity and ellipticity
- Feasibility is demonstrated with noise recordings from multiple sites and validated with results from other studies.

Corresponding author: Claudia Finger, `claudia.finger@ieg.fraunhofer.de`

Abstract

To integrate structural subsurface models and smooth seismic velocity models, they need to share common features and resolutions. Here, we propose a new approach for estimating the depth of sudden velocity changes from ambient-noise multi-mode Rayleigh waves applicable to a wide range of frequencies. Approximating the size and shape of the so-called energy ellipse at frequencies where the ellipticity has an extremum allows us to derive the depth of sudden velocity changes as the half height of the energy ellipse. We test our approach theoretically, numerically, and on real data from two geothermal sites by extracting Rayleigh wave ellipticities and phase velocities from three-component beamforming of ambient noise using the python code package B3AMpy. For a small-scale array, our approach validates the depth of quaternary sediments predicted by geological models. For deeper velocity changes, high uncertainties remain but the general trend of inclining boundaries can be recovered well. We demonstrate that, if impedance contrasts are larger than three, our approach is valid for multiple layers, laterally heterogeneous models, and a wide range of Poisson ratios.

Plain Language Summary

To effectively combine structural models and seismic velocity models, we've developed a new method. It estimates the depth of sudden changes in seismic velocity using Rayleigh waves from ambient noise. By analyzing extreme points in Rayleigh wave ellipticity, we determine the depth from the observed phase velocity at that point. We tested the method and found it works well for various scenarios, including multiple layers, heterogeneous models, and different material properties.

1 Introduction

Accurate representations of the subsurface are crucial for exploring natural resources, such as geothermal or hydrocarbon reservoirs, and estimating associated risks. Subsurface geophysical models can be structural, i.e., containing locations of faults and discontinuities, or represent a smooth spatial distribution of properties, i.e., as in seismic velocity models. Information from both types of models are crucial for estimating reservoir extends, and hence their economic viability, and accurately locating (micro-) seismicity to estimate and monitor the seismic hazard. Thus, structural and velocity models should ultimately be integrated into a common subsurface model that simultaneously includes smooth variations and sudden changes of elastic properties.

Active seismic surveys are widely used to obtain high-resolution structural models but are challenged by high costs and permitting issues, especially in urban areas. Earthquake tomographies can be used to constrain seismic velocities between hypocenters and seismic stations but require an adequate distribution of local seismic events to fully illuminate the subsurface (Toledo, 2020). Ambient seismic noise methods can image the subsurface regardless of the local seismicity level and without the need for active seismic sources. Although body waves have recently been identified in ambient noise recordings (Brenguier et al., 2019), most studies invert velocity profiles from surface wave dispersion curves (Löer et al., 2020; Galetti et al., 2017). However, the large wavelengths of low-frequency surface waves increase uncertainties at greater depths and result in smooth and gradient-like velocity models that lack sharp features. Thus, integration of active and passive methods is challenging due to different geometries, different frequencies, and a lack in common features to validate the integration. In this study, we aim to close the gap between active and passive subsurface models by retrieving structural information, i.e., the depth of major sudden velocity changes, from ambient noise Rayleigh waves. In contrast to other methods, such as horizontal-to-vertical spectral ratios (HVSR, (Bonnefoy-Claudet et al., 2006)), our approach does not rely on velocity information from secondary

studies and does not make prior assumptions about the wave types in seismic recordings. No inversion is needed to determine a preliminary depth estimate using our approach.

Several studies jointly inverted Rayleigh wave phase velocities and ellipticities for shallow (Picozzi et al., 2005) and deep (Berg et al., 2018) velocity models. If Rayleigh waves dominate the analysed frequency range, the horizontal-to-vertical spectral ratio (HVSR) curve closely resembles Rayleigh wave ellipticities (Fäh et al., 2008). The peak frequency of HVSR together with an estimate of the average shear velocity of the sediments can be used to estimate the thickness of sediments overlaying a stiffer bedrock, if the impedance contrast is larger than three (Bonnefoy-Claudet et al., 2006; Bard & Team, 2004). However, the accuracy of the depth estimate of HVSR strongly relies on accurate estimates of the shear-wave velocity. Since HVSR is typically applied to short recordings from single surface stations, sensitivity is in practice often limited to frequency ranges above 0.1 Hz and, thus, is limited to depths of about one hundred meters. It is assumed that the subsurface can be represented with a one-dimensional velocity profile. HVSR applied to single station recordings and to ambient-noise cross-correlations (Berg et al., 2018; Lin et al., 2012) are challenged by misidentifying wave types and modes. Thus, there is a need for a method that does not inherently assume the dominance of Rayleigh waves and works in a larger frequency range to image larger depth ranges.

In this study, we propose a new relation to estimate the depth of sudden velocity changes whenever phase velocity and ellipticity can be resolved over the same frequency range. We observe that Rayleigh wave ellipticities together with their phase velocities at particular frequencies can be used to estimate the depth of a velocity increase. The relationship we found seems to describe what we call an *energy ellipse* whose half height coincides with the depth of the velocity change. We validate the proposed approach using analytical approximations and a variety of one-dimensional velocity models. Three-component (3C) ambient noise beamforming at multiple seismic stations provides phase velocity and ellipticity of retrograde and prograde Rayleigh waves. We use the python code package B3AMpy (Finger & Löer, 2023; Löer & Finger, 2022) to perform 3C beamforming. The depth sensitivity depends mainly on the array geometry. We demonstrate the application of our new approach by applying 3C beamforming to synthetic waveforms and recorded waveforms from three seismic arrays at two sites. We find good agreements between our depth estimates and available depth estimates from active surveys and geological models. The accuracy of our new approach is comparable to HVSR results assuming the shear-wave velocity is perfectly known but is applicable to a wider depth range without prior assumptions or input from secondary studies.

2 Estimating the depth of sudden velocity changes using Rayleigh waves

Rayleigh waves propagating along the Earth's surface can be described with their direction of propagation (backazimuth ϕ), their frequency f, their horizontal propagation velocity (phase velocity v_{ph}) and their ellipticity e, that is the ratio of horizontal to vertical motion. The phase velocity v_{ph} is slightly smaller than the shear wave velocity v_s of the propagation medium (Aki & Richards, 1980). Ellipticity e mainly depends on the ratio of compressional wave speed to shear wave speed $\frac{v_p}{v_s}$ (Tuan et al., 2011) and is described as the ratio of horizontal to vertical particle motion $e = \frac{H}{V}$ (e.g., Herrmann, 2013). Both v_{ph} and e are frequency-dependent in non-homogeneous media and strongly influenced by step-wise velocity increases with depth (Boaga et al., 2013).

In homogeneous Poisson media, Rayleigh wave motion is elliptical and retrograde at the surface and inverts to prograde motion at greater depths. A particle at the surface is displaced in vertical and horizontal direction with peak motions shifted in phase by $\frac{\pi}{2}$ and with particle velocities in the nm to mm range. $e = \frac{H}{V}$ is smaller than one in homogeneous Poisson solids. The energy of a passing Rayleigh wave induces the displacement of all particles in a subvolume, which describes an elliptical motion visible in

the two-dimensional snapshots of the displacement wavefield (Figure 1 a and b). We refer to this as the energy ellipse. The size and shape of this energy ellipse can be calculated using the horizontal propagation velocity, i.e., the phase velocity v_{ph}, and frequency f of the Rayleigh wave as shown in the following. Both the ellipse of the particle motion at the surface and the energy ellipse have the same ellipticity e.

The wavelength $\lambda_R = \frac{v_{ph}}{f}$ of Rayleigh waves can be understood as the circumference of the energy ellipse, approximated as $C_e = \pi\sqrt{2(r_v^2 + r_h^2)}$, with r_v and r_h being the length of the major and minor half-axis of the ellipse. For both vertical and horizontal ellipses (Figure 1) r_v is the vertical half axis and $e = \frac{r_h}{r_v}$. An auxiliary circle with circumference C_e has a radius $r_v^{'} = \frac{C_e}{2\pi}$ (orange circles in Figure 1c). The difference between r_v of the ellipse and $r_v^{'}$ of the circle is the factor $\sqrt{\frac{2}{1+e^2}}$ representing the difference between circle and ellipse. $r_v^{'}$ is smaller than r_v if $e < 1$ and vice versa for $e > 1$ (Figure 1c). In practice, e is not well resolved over broad frequency ranges. Thus, assuming $r_v \approx r_v^{'}$, we can use the auxiliary circle to calculate the half-height of the energy ellipse r_v without explicitly using e:

$$r_v = \frac{v_{ph}}{2\pi f}, \tag{1}$$

with v_{ph} being the tangential velocity $v_t = r\omega$ at each point on the auxiliary circle and $\omega = 2\pi f$ being the angular velocity. Using $e = \frac{r_h}{r_v}$, we can estimate the half width of the energy ellipse as

$$r_h = r_v e = \frac{v_{ph} e}{2\pi f}. \tag{2}$$

For one-dimensional velocity profiles, v_{ph} and e can be estimated using Computer Programs in Seismology (CPS) (Herrmann, 2013). For a two-layer velocity model with a sudden velocity increase in a depth of $d = 1\,\mathrm{km}$ and $\frac{v_p}{v_s} = \sqrt{3}$ (Figure 2a), v_{ph} and $e = \frac{H}{V}$ are shown in Figure 2 b and c, respectively. The fundamental mode (superscript 0) and the first higher mode (superscript 1) are shown. Using equations 1 and 2, the size of the energy ellipse can be calculated (Figure 2d). The empirical relation $d_{HVSR} = \frac{v_s^1}{4 f_p^0}$ typically used to estimate the depth of sudden velocity changes in HVSR studies (Bonnefoy-Claudet et al., 2006)is plotted for comparison using the true shear-wave velocity v_s^1 given in the analytical model (Figure 2a).

At high frequencies, the fundamental mode (mode 0) is polarised vertically ($\frac{H}{V} < 1$) and both radii are smaller than the depth of the sudden velocity increase, $r_v > r_h << d$ (Figure 2d). With decreasing frequency, the radii increase with different rates until they have equal length, $r_h = r_v, e = 1$, here at $f_e^0 = f_p^1 = 0.57\,\mathrm{Hz}$, where f_e^0 is the frequency where the fundamental mode Rayleigh wave has an ellipticity of one and f_p^1 is the frequency where the first higher mode has a minimum in ellipticity. The deeper part of the Rayleigh wave already 'sees' the higher velocities at greater depths which causes different growth rates for r_v and r_h. For lower frequencies, $f < f_e^0$, one radius is larger than the depth of the velocity increase and the other is smaller than the depth of the velocity increase. If the shear velocity of the bottom layer is larger than the compressional velocity of the top layer, the ellipse changes to being horizontally polarised, $r_v < r_h$ (cf. Figure 1c right horizontal ellipse). Note that r_v and r_h are still calculated using v_{ph} (equations 1 and 2) but the ellipticity is now larger than one, $e > 1$, resulting in $r_h > r_v$. The two radii then increase at different rates for decreasing frequencies until r_v is equal to the depth of the sudden velocity increase, $r_v = d$ (Figure 2d). At this frequency, here at $f_p^0 = 0.43\,\mathrm{Hz}$, where e of the fundamental mode has reached its maximum, r_v is about equal to the depth of the sudden velocity increase. At even smaller frequencies, the radius of the second circle is larger than d and 'sees' the bottom layer velocities as well. e is declining again until the sensitivity of the energy ellipse is mostly to the deeper layer.

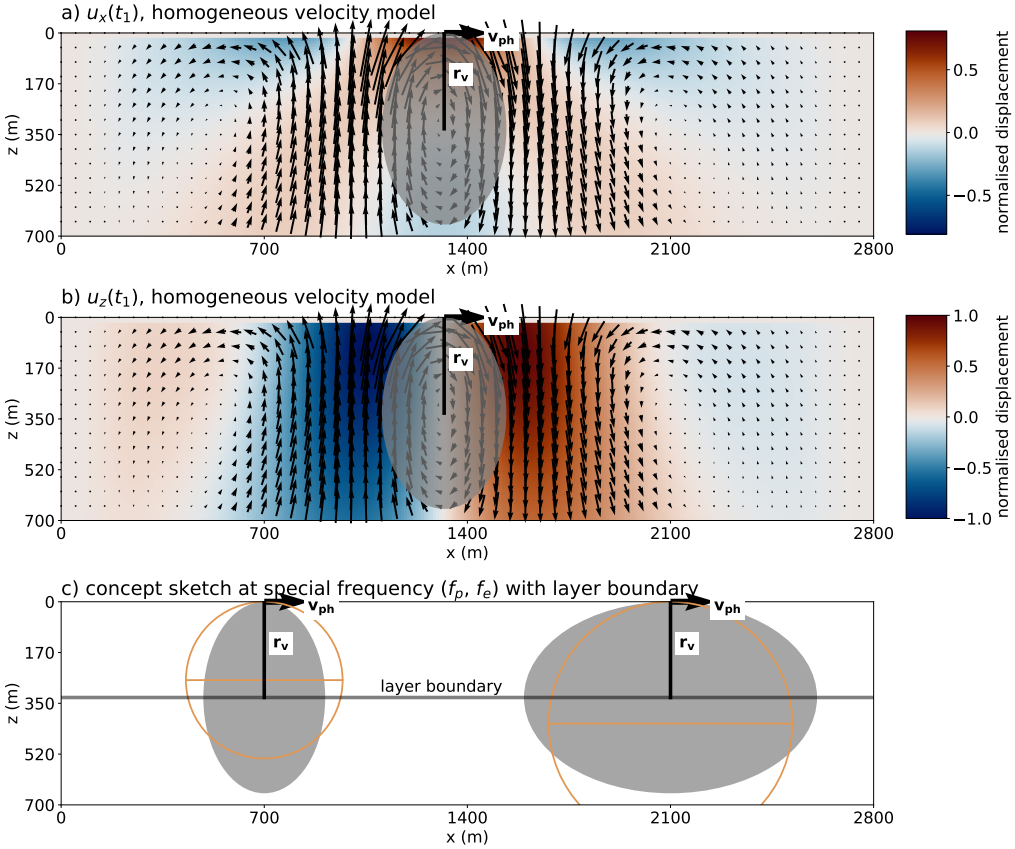

Figure 1. Snapshots of displacement in a) x direction and b) z direction for Rayleigh wave propagating in a homogeneous velocity model. Snapshots were created with a rotated staggered-grid finite difference scheme (Saenger et al., 2000). Energy ellipse is shaded grey. c) Sketch illustrating the estimation of the depth of a layer boundary as the half height of ellipse using the auxiliary circle (orange).

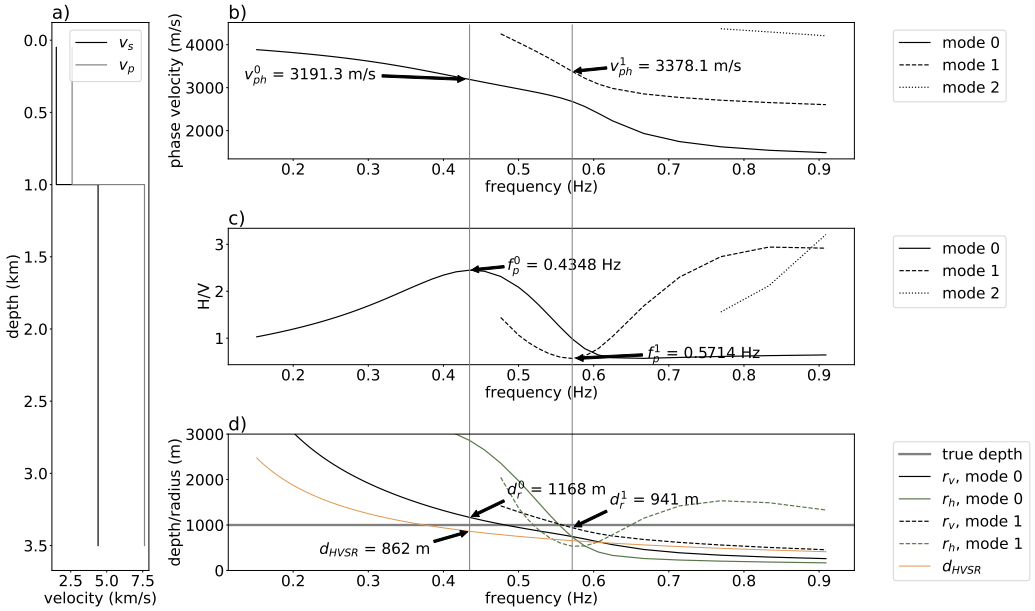

Figure 2. a) Input one-dimensional velocity model for analytical approximation of multi-mode Rayleigh wave b) phase velocity v_{ph} and c) ellipticity $e = \frac{H}{V}$ using (Herrmann, 2013). d) r_h and r_v calculated from b) and c) using equations 1 and 2. The empirical relation $d_{HVSR} = \frac{v_s^1}{4f_p}$, typically used in HVSR studies is plotted for comparison. Horizontal grey lines show frequencies where the fundamental and first higher mode experience extrema in ellipticity.

For the first higher mode (mode 1), a similar change can be observed (Figure 2d). The first higher mode is horizontally polarised for high frequencies with r_h being larger than the depth of the interface and r_v being smaller. With decreasing frequencies, r_v becomes as large as the depth of the sudden velocity increase with e being minimal, here at $f_p^1 = 0.57\,\text{Hz}$. Thus, we can also infer d from the first higher mode Rayleigh wave using equation 1 and the frequency f_p^1 where e of the first higher mode has a minimum. Note that in this case, the frequency where the fundamental mode Rayleigh wave is circular is equal to the frequency where the first higher mode has its minimum ellipticity ($f_p^1 = f_e^0$). Thus, this frequency can also be derived from the fundamental mode ellipticities which is beneficial since higher mode ellipticies are challenging to observe. However, for more complex velocity models, f_p^1 and f_e^0 may not coincide.

The depth estimates obtained from the fundamental and first higher mode are in this case $r_v^0(f_p^0) = 1168\,\text{m}$ and $r_v^1(f_p^1) = 941\,\text{m}$. Since the fundamental mode is horizontal at f_p^0 and the first higher mode is vertical at f_p^1 one value underestimates the depth and the other overestimates it (Figure 1c). The average depth estimate is, thus, 1054.5 m, a deviation of 5.5 % compared to the true depth. The depth estimate from the empirical relation typically used in horizontal-to-vertical spectral ratio (HVSR) studies (Bonnefoy-Claudet et al., 2006) is $d_{HVSR} = \frac{v_s^1}{4f_p^0} = \frac{1500\,\text{m/s]}}{4 \cdot 0.4348\,\text{Hz}} = 862\,\text{m}$, a deviation of more than 10 % based on the assumption that v_s^1 is known. Thus, our new approach is more accurate than HVSR in this case. Note that the depth estimate using the first higher mode is slightly more accurate than the one using the fundamental mode only.

Our proposed approach relies on the existence of horizontally polarised Rayleigh waves and works best if the first higher mode of Rayleigh waves exists at investigated frequencies. As described above, the fundamental Rayleigh wave becomes horizontally

polarised when the shear-wave velocity of the bottom layer is larger than the compressional-wave velocity of the shallower layer, $v_s^2 > v_p^1$. Assuming a poisson solid, i.e. $\frac{v_p}{v_s} = \sqrt{3}$, and densities of sandstone (about $\rho^1 = 2\,\mathrm{g/cm^3}$) and granite (about $\rho^2 = 2.63\,\mathrm{g/cm^3}$), the shear wave impedance contrast, $IC = \frac{rho^2 v_s^2}{rho^1 v_s^1}$ needs to be larger than 2.77 for v_s^2 to be larger than v_p^1. In our example velocity model (Figure 2) , the impedance contrast is four. For HVSR studies, a minimum impedance contrast of three is typically reported (Bonnefoy-Claudet et al., 2006). We tested different IC by changing v_s^2 (Figure 3a-d). For $IC = 2$ the first higher mode does not exist at lower frequencies and the peak in ellipticity of the fundamental mode is very small. Thus, the uncertainty of picking f_p^0 is high in this case and the deviation from the true source depth is high. We conclude that our method is valid for impedance contrasts larger than three. Note that only for $IC = 4$ is $r_v^1(f_p^1) = r_v^1(f_e^0)$ (Figure **??**d). An average from both modes would results in the most accurate depth estimate.

In the presence of fluids, the $\frac{v_p}{v_s}$-ratio can increase. Testing different $\frac{v_p}{v_s}$-ratios for both layers and using a constant impedance contrast of four reveals that with increasing $\frac{v_p}{v_s}$-ratio the phase velocities of the two modes become closer and mode mis-identification becomes more likely (Figure 3e). The frequency where the velocities of the two modes are closest together is very close to $f_e^0 = f_p^1$. This frequency is also referred to as the osculation frequency (Boaga et al., 2013). We can estimate the true depth of the sudden velocity increase relatively well for all tested $\frac{v_p}{v_s}$-ratios (Figure 3e-h). Note that also in these cases, the first higher mode provides more accurate depth estimates for a wider range of models than the fundamental mode and the depth estimate from HVSR (Figure 3h).

Adding an additional layer with varying impedance contrasts to the one-dimensional models reveals that the stronger impedance contrast tends to be retrieved. If the impedance contrasts of both velocity increases is the same, the depth estimate is closer to the deeper velocity increase (Figure 4). If the stronger impedance contrast is shallower (Figure 4e-h), the shallower layer boundary can be retrieved accurately using $r_v^1(f_e^0)$. If the stronger impedance contrast is deeper (Figure 4a-d), $r_v^1(f_e^0)$ retrieves the stronger shallower contrast if the impedance contrast is larger than three. Low velocity zones can occur and are thus an important consideration. Reducing the velocity of the middle layer (not shown), reveals that deviations from the true depth are higher but a rough estimate of the depth of the larger, in our case deeper, velocity increase is still possible.

3 Three-component ambient-noise beamforming of Rayleigh waves

To estimate the depth of sudden velocity increases using equation 1, we need to estimate v_{ph} and e over the desired frequency range. We choose Beamforming of three-component ambient noise (B3AM, (Löer & Finger, 2022)) for its distinct advantages of identifying wave types in small time windows of continuous waveforms and producing v_{ph} and e at the same discrete frequencies. Results from all processed time windows can be analysed statistically to obtain v_{ph} and e against frequency averaged over longer time windows. B3AM processes three-component waveforms recorded with multiple seismic stations and enables to identify prograde and retrograde Rayleigh waves separately, which allows a first indication of mode separation.

B3AM compares observed three-component phase shifts S^{3C} between stations of an array and between components of a station to theoretical phase shifts $a(k, \theta, \xi)$ created over a pre-defined grid of wavenumber k, backazimuth θ and polarisation parameters ξ. Backazimuth θ is defined as counter-clockwise from East. Polarisation parameters considered are the dip (inclination angle of body waves), the rotation around the x axis (i.e. for differentiating prograde and retrograde Rayleigh waves) and the ellipticity e^B defined in the range $[0, 2]$ with zero referring to a linear horizontal polarization, one referring to a circular polarisation and two referring to a linear vertical polarization.

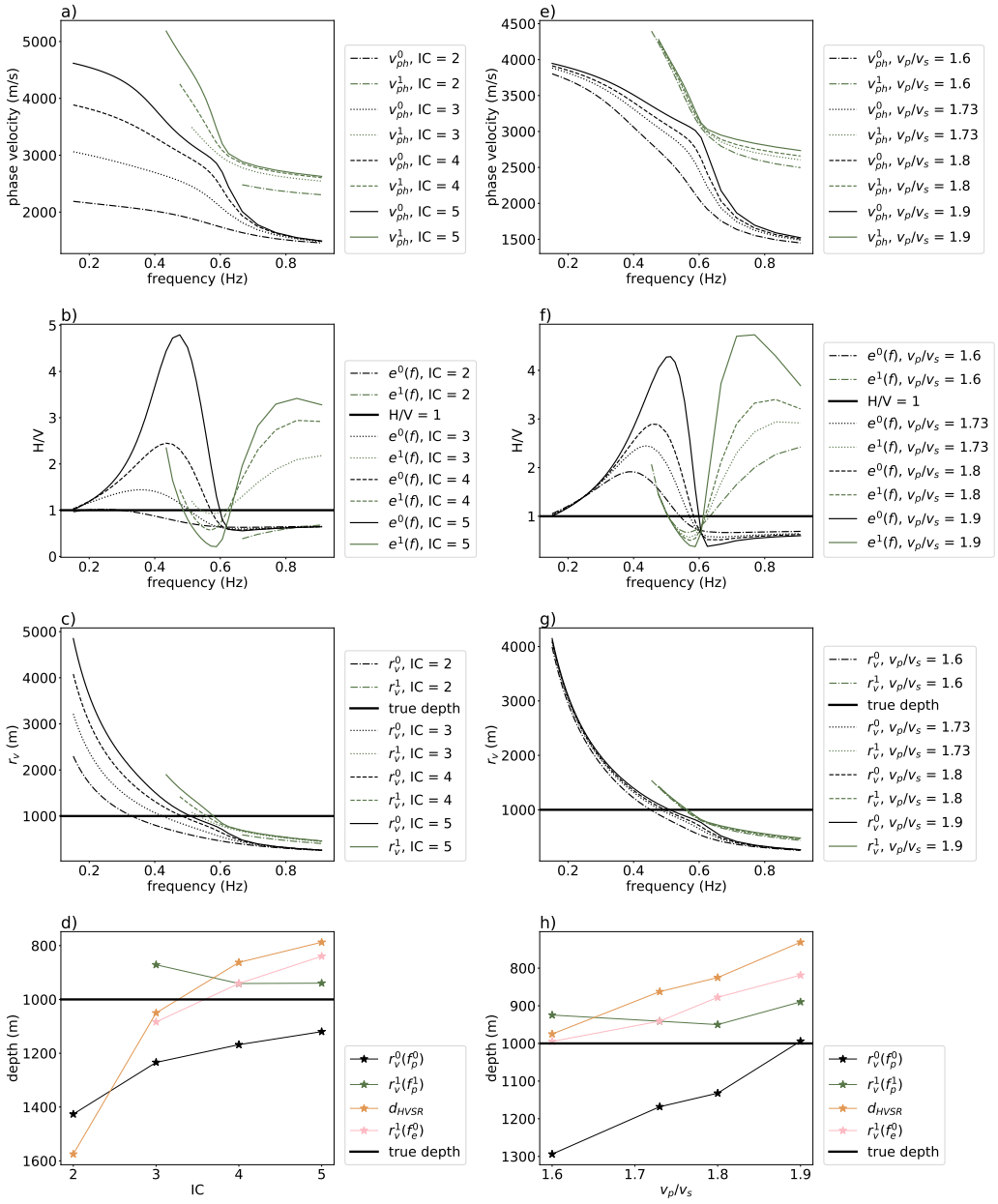

Figure 3. Phase velocity v_{ph}, H/V, r_v, and deviation to true depth for different types of theoretical velocity models. In a) to d) the impedance contrast IC between two layers is varied. In e) to h), the $\frac{v_p}{v_s}$-ratio is varied simultaneously for both layers and the impedance contrast is kept constant at $IC = 4$.

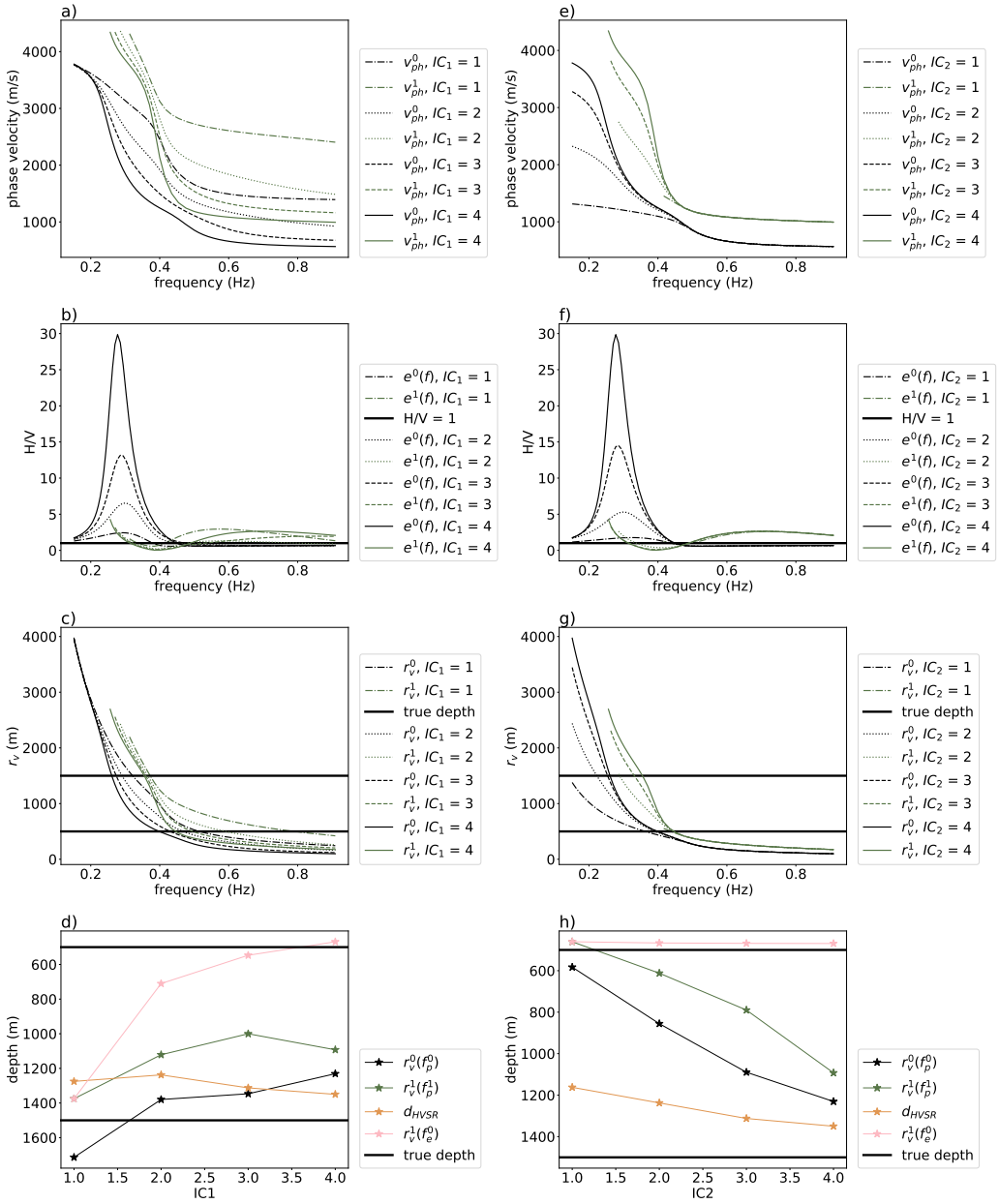

Figure 4. Phase velocity v_{ph}, H/V, r_v, and deviation to true depth for different types of theoretical velocity models. In a) to d), the impedance contrast of the shallower of two layer boundaries is varied while $\frac{v_p}{v_s} = 1.73$ and $IC = 4$. In e) to h), the impedance contrast of the deeper of the two layer boundaries is varied.

We can convert the ellipticity of B3AM to the more standardised definition using:

$$e = H/V = 2 - e^B, e^B \geq 1 \tag{3}$$

$$e = H/V = \frac{1}{e^B}, e^B \leq 1 \tag{4}$$

Further details about the used code can be found in (Löer & Finger, 2022).

Apart from detrending, demeaning and removal of instrument response, pre-processing should be kept to a minimum to avoid introducing artificial phase shifts. For the low frequency examples in this study (large station network in Wesweiler and station network in UtahFORGE), some pre-processing is required to obtain stable results for the low-frequency investigation. In these cases, we modify the running-mean time normalization proposed by (Bensen et al., 2007) to simultaneously weigh all three-component waveforms with the same weights calculated using one of the components. This is repeated with weights calculated over each component. Thus, relative amplitudes are always kept the same but spurious signals or earthquakes on each component are reduced in amplitude. No spectral whitening is applied to retain relative amplitudes between components and thus resolve ellipticities. Results from B3AM are normalised per frequency in post-processing to counteract unbalanced energy distributions across the frequencies.

As for all array methods, the wavenumber and frequency limits depend on the station geometry and subsurface velocities. We propose the following steps to determine the input parameters used to calculate the theoretical phase shifts in B3Am:

1. Plot the array response function (Löer et al., 2018) for multiple backazimuths and derive the minimum wavenumber k_{min} as the width of the central peak at half height and the maximum wavenumber k_{max} as the wavenumber where the first peak reaches half the height of the central peak as proposed by Wathelet et al. (2008). We consider k_{min} to represent the resolution limit, i.e. the smallest distinguishable wavenumbers, and use a wavenumber minimum of zero in B3AM to allow detection of vertical incident body waves. We found that using $k_{max}/2$ as the upper wavenumber limit works well in keeping the total number of discrete wavenumbers and, thus, the computation time low but obtaining high resolution in the well-resolved wavenumber parts.
2. Derive the desired wavenumber sampling Δk to achieve the desired depth sampling Δr. Since Δk and Δr are inversely related (equation 1), sampling of r_v is non-linear (Figure 5a). We recommend to severely oversample the wavenumber to artificially increase the radius sampling and reduce the wavenumber sampling through smoothing of the B3AM results in post-processing.
3. Make an educated guess about expected subsurface velocities (v_{min}, v_{max}) in the resolvable depth range estimated using k_{min} and k_{max} in equation 1.
4. Determine frequency range from wavenumber and velocity range. The minimum frequency $f_{min} = v_{max}k_{min}$ results from the highest expected velocity and the minimum resolvable wavenumber. The maximum frequency $f_{max} = v_{min}k_{max}$ results from the minimum expected frequency and the maximum resolvable wavenumber. Combining these limits defines the resolvable value range (Figure 5b).
5. Determine the desired frequency sampling and time window length for analyses based on the largest Period $T_{max} = \frac{1}{f_{min}}$. We use time window lengths of $4T_{max}$ and windows with 50 % overlap.

In this study, we sample e^B linearly with a spacing of 0.01. This results in equal weighting of horizontal and vertical Rayleigh waves but is different from e.g. HVSR curves where the horizontal part is usually sampled higher or exaggerated when plotting. The advantage of linearly sampling e^B is the ease of picking f_e^0. With our chosen e^B sampling, we can resolve H/V amplitudes from 0.01 to 100 with most precision for $H/V <$ 10.

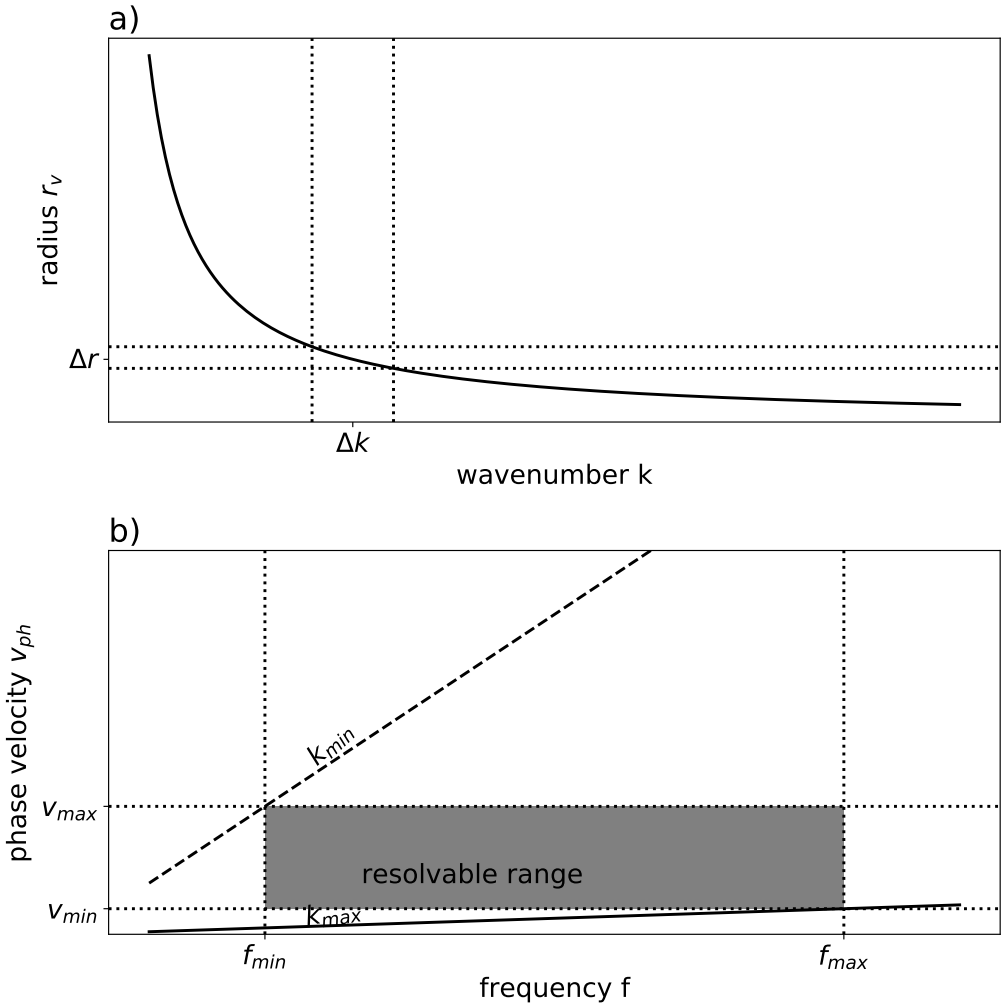

Figure 5. a) Relation between wavenumber sampling and radius r_v (equation 1). b) Relation between wavenumber, frequency and velocity limits and resolvable value range in B3AM.

B3AM provides wave type, polarisation parameters ξ and horizontal wavenumber k_h for every short time window per discrete frequency f. The propagation velocity for Rayleigh waves can be calculated as $v_{ph} = \frac{f}{k_h}$. B3AM results contain velocities outside the expected velocity range due to constant wavenumber sampling (Figure 5b). Thus, we manually exclude results with velocities smaller than v_{min} and larger than v_{max}. We then select only results identified by the polarization parameters as retrograde or prograde Rayleigh waves and calculate two-dimensional histograms of e^B and k_h over f. We smooth the histograms and pick the maximum per frequency and determine the uncertainty as the width of the local peak at half height. Some cases require manual correction of automatic picks which is indicated for the individual results. We calculate $r_v(f) = \frac{1}{2\pi k_h(f)}$ directly from the picked wavenumbers for all frequencies and pick f_p and f_e for all visible modes from the ellipticity curves. We determine the depth of velocity increases as $r_v(f_{p/e})$. Propagating relative errors from the wavenumber histograms to the depth estimates directly provides an uncertainty for our depth estimate.

4 Feasibility test using synthetic waveforms

To validate our approach in a realistic but controlled setting, we computed three-component full-waveform ambient seismic waveforms using a rotated staggered-grid finite-difference scheme (Saenger et al., 2000). The continuous waveforms recorded at the receiver positions described below are available from Finger and Saenger (2023).

The goal of the numerical simulations is a waveform dataset with similar characteristics as observed ambient seismic noise. The main attribute of ambient seismic noise is its seemingly random nature. Waves with different properties arrive from different directions at the receivers. To maximise this randomness, we implement 8000 randomly located point sources with a Ricker source time function with random origin times, random moment tensor components and random dominant frequencies. We insert these random sources in a three-dimensional velocity model. The inner part of the model, 2.5 times the aperture of the receiver array in the center of the model, is kept free from sources to adhere to the plane wave assumption inherent to the beamforming approach. Frequencies are limited between 0.01 Hz and 2 Hz to avoid numerical dispersion and stability issues. A total of $1540\,\mathrm{s} \approx 26 min$ of computed waveforms are generated.

The model size is 60 km by 60 km with a total depth of 30 km to allow large wavelengths to exist. The grid spacing is 50 m in all directions and the timestep is 0.005 s, which results in a realistic sampling rate of 200 Hz. The top of the model is a free surface and the sides and the bottom of the model are absorbing boundaries. 441 receivers are distributed in a regular grid of 21 by 21 receivers at the center of the model at the free surface. The inter-receiver distance is 500 m. We test two velocity models: a) the same velocity as in Figure 2 extended laterally to three dimensions and b) the same velocities as in Figure 2 but with a layer boundary dipping towards east.

4.1 Velocity model with two horizontal layers

We apply B3AM to the 26 minutes of synthetic waveform data recorded with the 100 center receivers and apply the workflow outlined in section 3 to obtain the maximum wavenumber limit as $\frac{k_{max}}{2} = 0.0001\,\mathrm{m}^{-1}$ and the wavenumber resolution as $\frac{k_{min}}{2} = 3.5{\cdot}10^{-5}\,\mathrm{m}^{-1}$. We oversample the wavenumber using 200 values. With expected velocities of $v_{min} = 1000\,\mathrm{m/s}$ to $v_{max} = 5000\,\mathrm{m/s}$, the analysed frequency range is $f_{min} = 0.2\,\mathrm{Hz}$ and $f_{max} = 1\,\mathrm{Hz}$. The time window length is 20.48 s resulting in 148 total analysed time windows. The frequency sampling is $\Delta f = 0.0244\,\mathrm{Hz}$ resulting in 32 analysed frequencies.

The two-dimensional smoothed histograms of $e^B(f)$ (Figure 6a and b) and $k_h(f)$ (Figure 6d and e) are used to pick multi-mode dispersion and ellipticity curves. The ret-

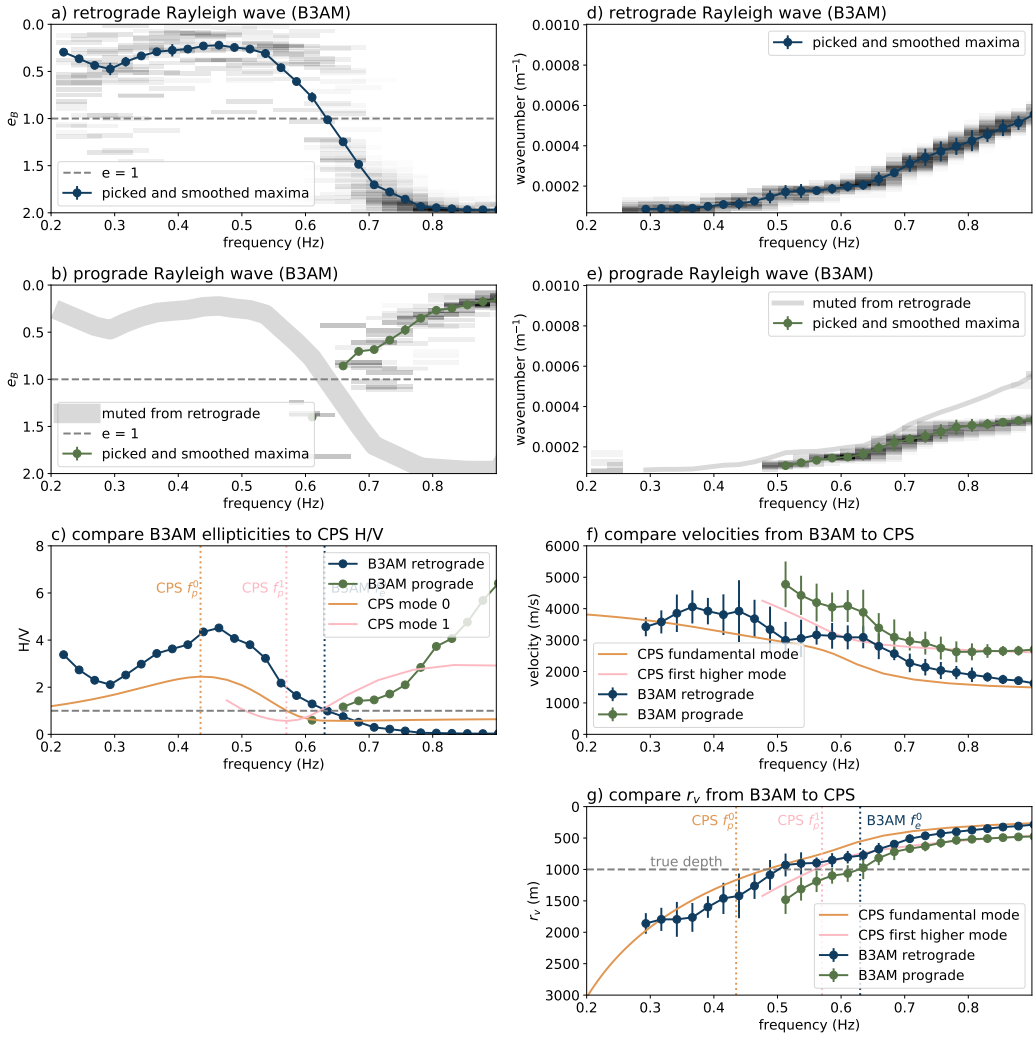

Figure 6. a) Histogram of $e^B(f)$ for retrograde Rayleigh waves from B3AM and picked and smoothed maxima. Uncertainties are too small to be visible. b) Histogram of $e^B(f)$ of prograde Rayleigh waves from B3AM and picked and smoothed maxima. c) Conversion of ellipticities to H/V and comparison to result from CPS. Vertical lines mark frequencies of extrema. d) Histogram of $k_h(f)$ of retrograde Rayleigh waves from B3AM and picked and smoothed maxima. e) Histogram of $k_h(f)$ of prograde Rayleigh waves from B3AM. f) Conversion from wavenumber to velocity and comparison to CPS. g) Half-height of Rayleigh wave energy ellipse r_v from B3AM and CPS results. Vertical lines show frequencies from c. Horizontal line shows true depth.

rograde ellipticities and wavenumbers can be picked unambiguously. The prograde ellipticities and wavenumbers are picked once the retrograde picks are removed from the prograde histograms. There is some ambiguity between retrograde and prograde waves. However, picked results from B3AM correspond relatively well to those from CPS (Figure 6c and f). As expected, the fundamental mode is retrograde and the first higher mode is prograde. Discrepancies in absolute values between B3AM results of the synthetic data and CPS results could stem from uncertainties of the approaches but do not alter the final depth estimates. Picking $f_e^0 = 0.63\,\mathrm{Hz}$ from B3AM and estimating the depth of the sudden velocity change as $r_v^1(f_e^0)$ results in a depth estimate of $973.6\,\mathrm{m} \pm 356.1\,\mathrm{m}$, a deviation of less than 3% to the true depth.

4.2 Velocity model with inclined layer boundary

We apply B3AM to the 26 minutes of continuous synthetic waveform data created with the inclined-layer velocity model. We analyse 100 receivers at a time and then move all receivers one receiver over to analyse the next 100 receivers. In this manner, we analyse a total of 12 subsets of receivers. We use the same parameters for B3AM as for the previous case and estimate the depth of the velocity increase from $r_v^1(f_e^0)$, the half height of the prograde Rayleigh wave energy ellipse at f_e^0, the frequency where the retrograde Rayleigh wave is circular. We find a good agreement of true and estimated depth across all subarrays (Figure 7) with deviations of less than 10% for half of the subarrays. B3AM seems to generally overestimate the depth in this case. Variations in depth estimate accuracy could result from uncertainty in picking. We only analysed 32 discrete frequencies. For some cases, differences between subarrays are smaller than the resolution. Additionally, the backazimuth of the Rayleigh waves could influence if the depth is under- or overestimated if the velocity model varies laterally. We investigated the prominent backazimuth for each subarray but could not find a clear correlation to the depth estimate deviation. The footprint of the array, here 4.5 km, does not seem to influence results and depth estimates sem to be an average over the footprint. Therefore, we conclude that the deviation stems mostly from the inherent uncertainties of the method.

5 Application to recorded ambient noise

We apply the developed workflow to two seismic station deployments. At the geothermal test site UtahFORGE in Utah, USA, reflection seismic data show a strong impedance contrast between sediments and the granitoid bedrock (Podgorney, 2020). We use this to validate our approach in a real world scenario. In Western Germany surrounding the town of Eschweiler-Weisweiler, no active seismic surveys have been performed and, thus, geological models (Fritschle et al., 2021) have large uncertainties. Our approach gives the first analysis into the deeper subsurface.

5.1 Application site UtahFORGE, USA

In December 2016, 49 Fairfield Nodal Zland three-component (3C) geophones were deployed in a regular grid with 600 m inter-station spacing at the geothermal site UtahFORGE in Utah, USA (Pankow, 2016). We analyse 48 hours of continuous waveform data on 20.12.2016 and 21.12.2016 using four subsets of 16 receivers each. We restricted the upper wavenumber limit to $k_{max} = 0.0004\,\mathrm{m}^{-1}$ and the frequency range from 0.05 Hz to 0.5 Hz for maximum sensitivity in the expected depth range. Raw waveforms are preprocessed with the modified moving average time normalisation as described in section 3 for more stable results. Ellipticities and wavenumbers showed large uncertainties that made picking challenging. We manually had to revise the automatic picks. The B3AM results for the first 16-receiver subset is shown in Figure 8.

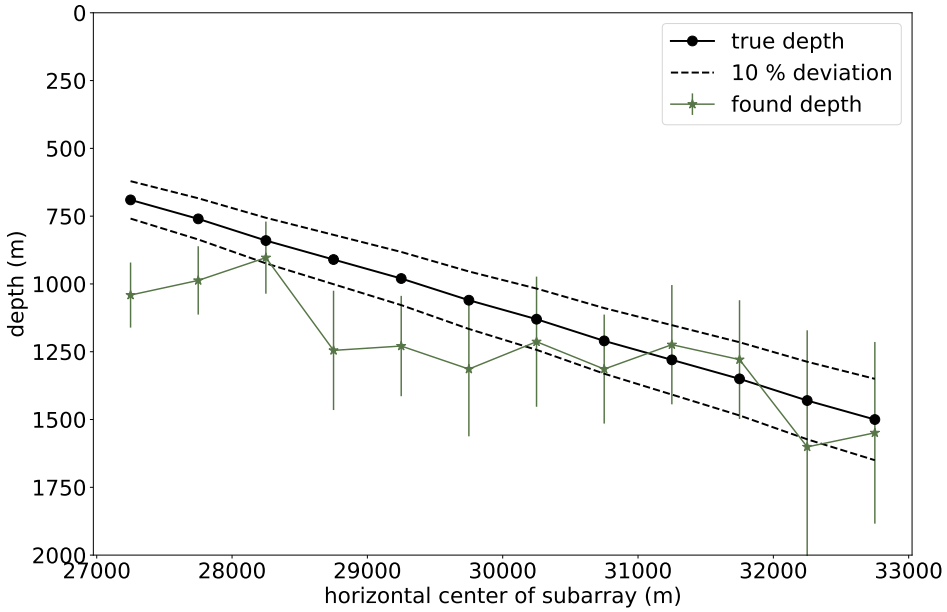

Figure 7. Estimated depth ($r_v^1(f_e^0)$) of sudden velocity increase derived using multiple subsets of receivers for the model with an inclined layer boundary.

Comparing the depth estimates from all four 16-receiver subsets to the depth of the granitoid boundary averaged in North-South direction as reported by (Podgorney, 2020) reveals that B3AM recovers the general trend of the inclined boundary well but overestimates the depth significantly. The lower limit of the uncertainty falls within the 50 % deviation. The regional velocity model derived from ambient-noise phase velocities and H/V ratios (Wells et al., 2022) reveals an extensive low velocity zone down to depths of about 2 km not taking the elevation into account. Assuming our approach is sensitive to this deeper velocity increase would mean that the deeper velocitiy increase is sharper than the sediment-to-granitoid boundary at shallower depths. Using estimated velocites from Zhang and Gao (2021) and typical densities for sandstone and granite, we estimate the shear impedance contrast of the sediment-to-granitoid interface to be $IC = \frac{2630\,\mathrm{kg/m^3}\,3000\,\mathrm{m/s}}{2000\,\mathrm{kg/m^3}2000\,\mathrm{m/s}} = 1.97$ and would, thus, be too small for our approach. Thus, we conclude that our approach may confirm a deeper increase in velocities.

5.2 Application site Weisweiler, Germany

Surrounding the town of Eschweiler-Weisweiler, in the western part of Germany, a small-scale short-term array has been deployed in June 2021 followed by a larger network consisting of among others 27 broadband seismic stations (Finger et al., 2023).

We analyse two hours of continuous waveform data recorded in the night of June 20th 2021 with the small-scale array with B3AM. The small array enables the analysis of wavenumbers up to $k_{max} = 0.023\,\mathrm{m}^{-1}$ in the frequency range of $f_{min} = 1\,\mathrm{Hz}$ to $f_{max} = 4.6\,\mathrm{Hz}$. B3AM results seem to be sensitive down to frequencies just above the peak frequency of HVSR curves (Figure 10c). This high-filtering effect has been observed in other studies as well (Scherbaum et al., 2003). Thus, the peak frequency of the fundamental mode cannot be resolved well in this case. However, f_e^0 can be clearly identified as 2.44 Hz.

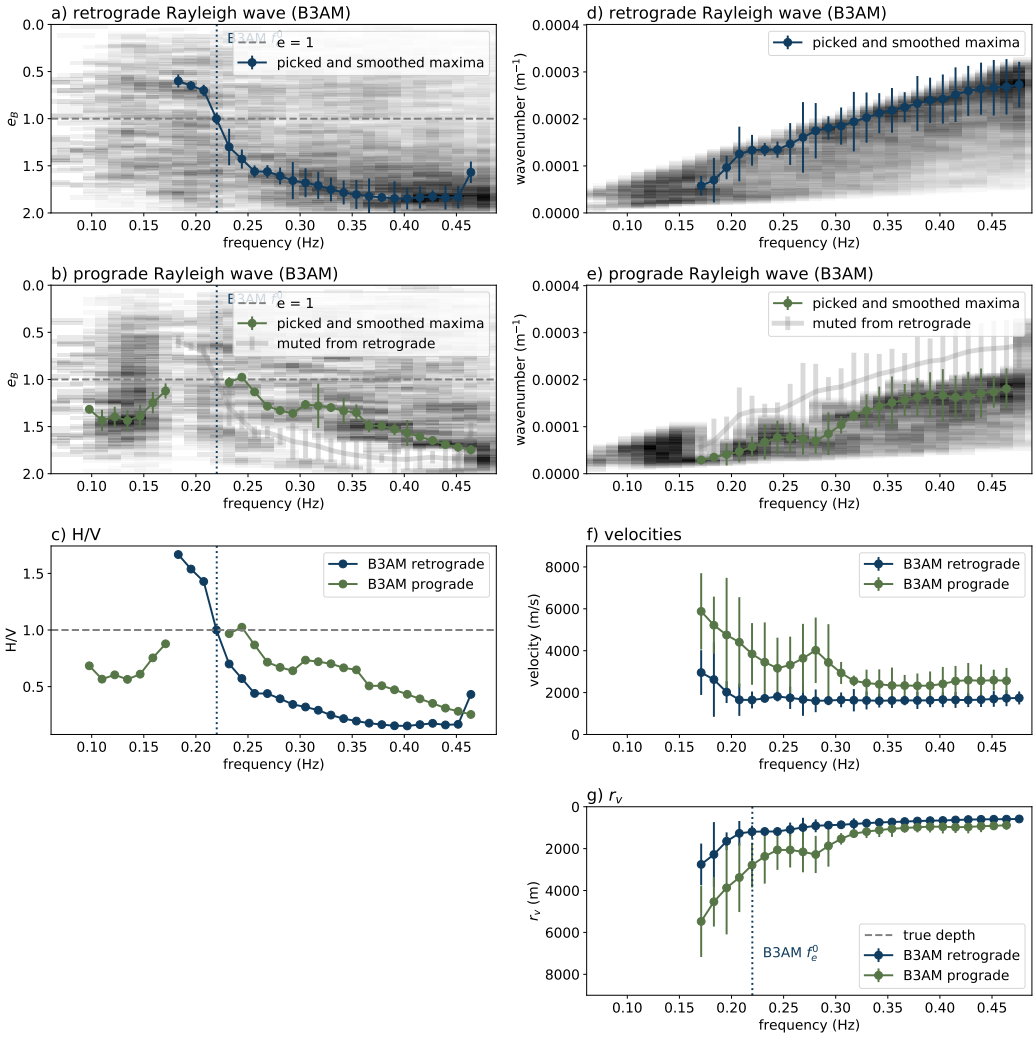

Figure 8. B3AM results of 48 hours of continuous data recorded with the first of four 16-receiver subsets of the Forge array. a) Ellipticities of retrograde Rayleigh wave, b) Ellipticities of prograde Rayleigh wave, c) Wavenumber of retrograde Rayleigh wave, d) Wavenumber of prograde Rayleigh wave. e) Half-height r_v of energy ellipse for retrograde and prograde Rayleigh wave.

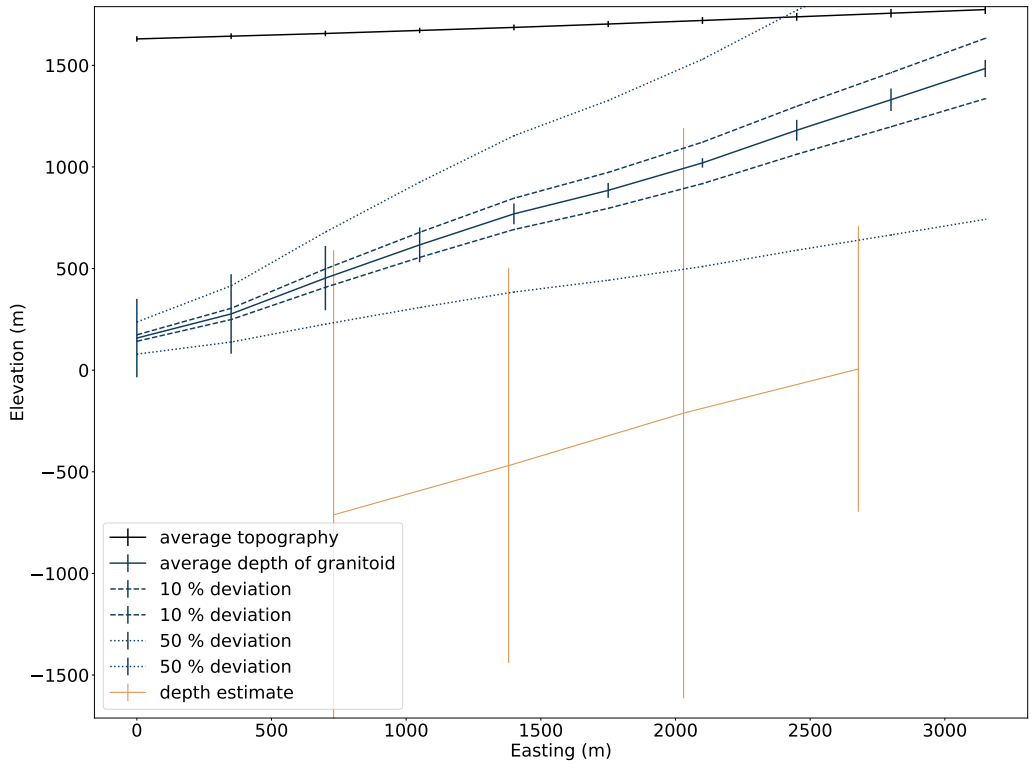

Figure 9. Depth estimates from all four 16-receiver subsets of the FORGE array compared to the topography and depth of the known granitoid boundary averaged in North-South direction.

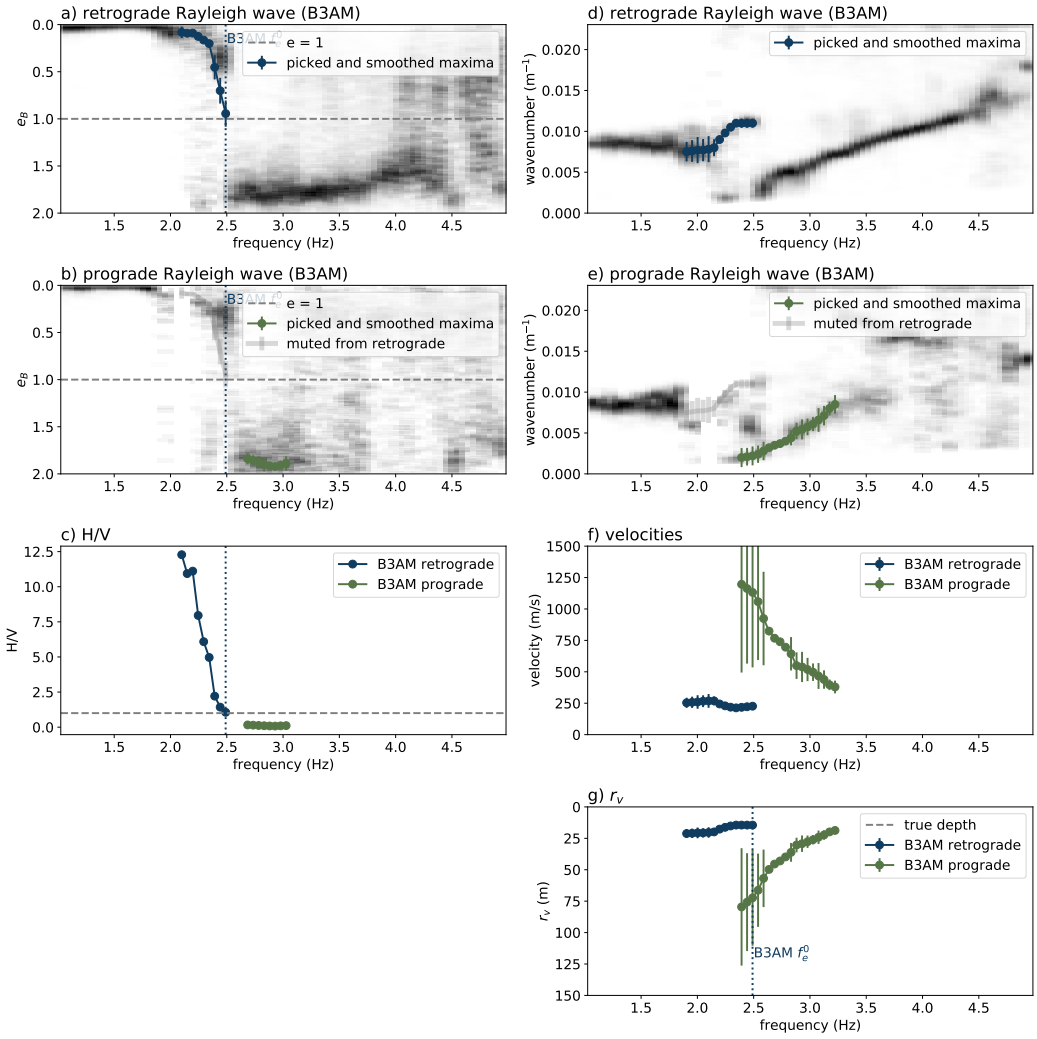

Figure 10. Results of retrograde and prograde Ralyeigh waves from B3AM for two hours of continuous noise data recorded with the seven stations of the small-scale network. Ellipticities of a) retrograde Rayleigh waves and b) prograde Rayleigh waves. Wavenumbers of c) retrograde and d) prograde Rayleigh waves. f) Half-height r_v of energy ellipse for retrograde and prograde Rayleigh waves. Vertical lines mark picked interesting frequencies in a - c used to estimate depth in f.

The prograde ellipticities have a minimum around 2.8 Hz. In the retrograde and prograde wavenumbers (Figure 10d and e), some mode leakage seems to occur. By manually picking modes in restricted frequency ranges allows to estimate the depth as $r_v^1(f_e^0 = 2.44\,\text{Hz}) = 72.3\,\text{m} \pm 29.9\,\text{m}$. This is in good agreement with geological models (Fritschle et al., 2021) that estimate a thickness of about 60 m for the quaternary sediments. Using the HVSR peak frequency of 1.6 Hz derived in Gotowik (2022) and the minimal shear velocity of 400 m/s estimated from our B3AM results, we get a depth estimate of $\frac{400\,\text{m/s}}{4 \cdot 1.6\,\text{Hz}} = 63\,\text{m}$ using the empirical HVSR equation.

For the large network in Weisweiler, we analyse 48 hours of continuous waveform data recorded at 23 of the broadband stations (Nanometrics Trillium 20s and 120s) that were recording with all components on 16.10.2021 and 17.10.2021. We use a maximum

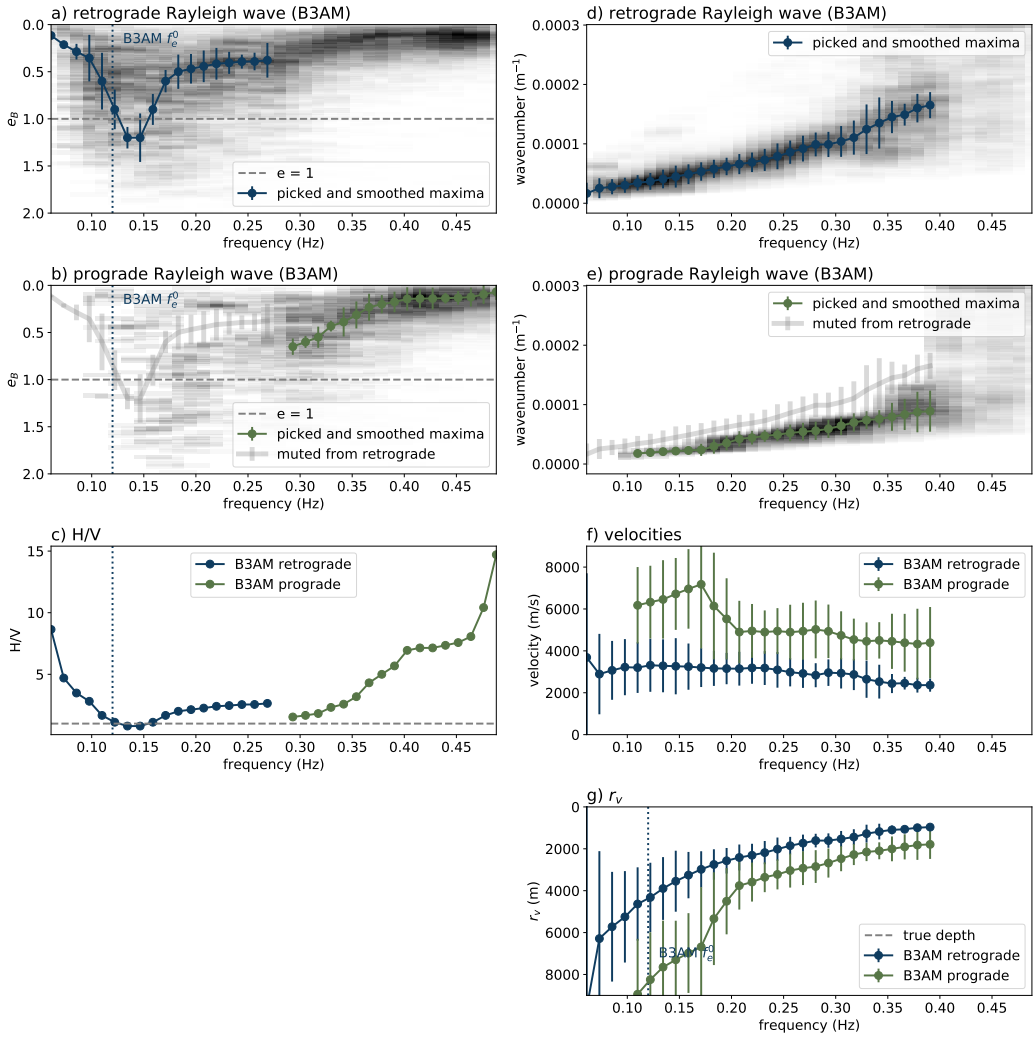

Figure 11. B3AM results of 48 hours of continuous data recorded with 23 stations of the large Weisweiler network. a) Ellipticities of retrograde Rayleigh wave, b) ellipticities of prograde Rayleigh wave, c) wavenumber of retrograde Rayleigh wave, d) wavenumber of prograde Rayleigh wave and e) half-height r_v of energy ellipse for retrograde and prograde Rayleigh wave.

wavenumber limit of $k_{max} = 0.0003\,\mathrm{m}^{-1}$. We analyse frequencies in the range of 0.05 Hz to 0.5 Hz and apply the modified running mean time normalization during pre-processing to get more stable results.

While wavenumbers are well-resolved (Figure 11d and e), ellipticities are not well resolved in this case (Figure 11a and b). Contrary to the simplified models in previous sections, mostly horizontal polarised ellipses seem to be found for the retrograde wave. However, at around 0.15 Hz the retrograde ellipticities seem to become vertical. If we assume that this is f_e^0, we can estimate a depth as $r_v^1(f_e^0)$ of more than 8 km (Figure 11e). This is deeper than any presently available models. The reported depth of the 'Massenkalk' in the geological models in (Fritschle et al., 2021) is about half of that depth. Alternatively assuming that the retrograde ellipticities represent the first higher mode in this case, we can pick $r_v^1(f_p^1) \approx 4\,\mathrm{km}$ but with high uncertainties. We tried to analyse subsets of receivers to observe lateral changes of this depth but uncertainties are too high

to make a robust estimate. Similarly as for the case in FORGE, we can conclude that shallower velocity changes have probably too small impedance contrasts for our approach. In this complex geological setting, our simplified approach to estimate the depth of sudden velocity changes might be too simplified to provide a robust estimate.

6 Discussion

We present here a new approach to derive the depth of sudden velocity changes from Rayleigh waves recorded at seismic station networks. If ellipticity and phase velocity of Rayleigh waves can be retrieved over the same frequency range, the depth can be estimated as the half height of the energy ellipse at the peak frequencies in ellipticity. This approach has been validated using analytical approximations for a multitude of velocity models. The depth can be estimated within reasonable uncertainties for impedance contrasts above three and different $\frac{v_p}{v_s}$-ratios. In all tested multi-layer models, the strongest impedance contrast is retrieved. This approach can be applied to any seismic recordings containing Rayleigh waves in the interesting frequency range. The prevalence of Rayleigh waves in ambient seismic noise is an advantage for statistically more stable results. In this study, we only applied it the method to surface observations but we can envision an application also to borehole stations with an adapted workflow.

We observe that wavenumbers can generally be better resolved than ellipticities using B3AM. This could be due to the assumption of perfect ellipses that are neither tilted nor distorted. This assumption does not hold true for lower frequencies sensitive to greater depths where velocities cannot be considered homogeneous anymore. Wavenumbers are resolved down to a frequency slightly above the peak frequency of fundamental mode ellipticities. This high-pass filtering effect caused by low-velocity layers overlaying high-velocity layers is a common phenomenon (Scherbaum et al., 2003). The large uncertainties in ellipticities, especially for lower frequencies, may be reduced by analysing more waveform data. Wavenumber uncertainty can be improved with denser station networks. Generally, uncertainties in depth estimates increase with decreasing frequency. With dense enough stations networks and high enough wavenumber sampling, these uncertainties are sufficiently small for an initial estimate of the depth of sudden velocity changes.

The ellipticity e_B in B3AM is linearly resolved between zero and two with higher resolution around $e_B = 1$. This enables the straight-forward identification of f_e^0. At this frequency, mode mis-identification is likely. Identifying f_e^0 thus helps in distinguishing modes and can alleviate some of the challenges in multi-mode dispersion curve analysis (Boaga et al., 2013). Calculating r_v additionally helps to understand the Rayleigh wave behaviour in complex velocity models and can give a first estimate of the depth of Rayleigh wave sensitivity. Our proposed approach benefits from multi-mode analysis of Rayleigh waves since depths are over- or underestimated depending on the orientation of the energy ellipse.

When velocity models are not strictly one dimensional, uncertainties can be high since waves arriving from different directions are influenced by different velocities. The resulting one-dimensional depth estimate is an average of velocities over the footprint of the array. The horizontal footprint of this method is a combination of the total used array size and the horizontal size r_h of the Rayleigh wave energy ellipse. We found that in the synthetic test cases, small lateral changes could be resolved by using overlapping subsets of receivers.

We see multiple possible uses of our proposed new relations:

- Determine osculation frequency (f_e^0) and, thus, aid in preventing mode misidentification when using Rayleigh wave dispersion curves.

- Estimate conversion from frequency to depth for Rayleigh wave phase and group velocity using r_v as an indicator for depth.
- Determine the depth of sudden high-impedance velocity changes for use as constraints in inversions of Rayleigh wave dispersion curves to constrain and validate geological models.
- Combine our approach with HVSR studies for increasing accuracy of shallow velocity structures.
- Use depth of sudden velocity changes to integrate passive and active seismic methods based on common (sub-) horizontal contrasts from both methods.

7 Conclusion

We present a new approach to estimate the depth of sudden velocity changes using seismic arrays that generally provides more accurate results than HVSR. Our approach is fully self-contained, i.e., no information from other studies needed, and does not rely on a priori assumptions about the wavefield. Approximation of the size of the energy ellipse enables a data-driven workflow for initial estimates of the depth of strong impedance contrasts. The capabilities of B3AM to identify and separate wave types from ambient-seismic noise recording enables multi-mode Rayleigh waves to be used in our approach and, thus, significantly increases the depth accuracy. We demonstrated the applicability at two sites in Utah, USA, and in Germany. While high uncertainties remain for the depth of deep velocity changes, this approach shows a high potential to increase accuracy of velocity models on multiple scales.

8 Open Research

The most recent version of the B3AM code for the python version used in this study can be downloaded from github (https://github.com/cl-finger/B3Ampy) with the version used in this study archived at Finger and Löer (2023). The numerical data created with the rotated staggered-grid finite difference code can be found at Finger and Saenger (2023). The nodal seismic data for Forge is available from (Pankow, 2016) and the depth of the granitoid boundary from (Podgorney, 2020). The passive seismic dataset recorded in Weisweiler, Germany can be obtained from (Finger et al., 2022). A detailed description of this dataset can be found in (Finger et al., 2023).

Acknowledgments

This project has been subsidized through the Cofund GEOTHERMICA, which is supported by the European Union's HORIZON 2020 programme for research, technological development and demonstration under grant agreement no. 731117 (DEEP). The german sub-project DEEP-SIGHT has been funded by the 'Bundesministerium für Wirtschaft und Klima' under project number 03EE4016. The authors gratefully acknowledge the Gauss Centre for Supercomputing e.V. (`http://www.gauss-centre.eu`, last access: 14 September 2023) for funding this project by providing computing time through the John von Neumann Institute for Computing (NIC) on the GCS Supercomputer JUWELS at Jülich Supercomputing Centre (JSC). We thank Erik H. Saenger for providing the finite-difference code HeidimodX.

References

Aki, K., & Richards, P. (1980). *Quantitative Seismology: Theory and Methods.* WH Freeman & Co.

Bard, P. Y., & Team. (2004). Guidelines for the implementation of the H/V spectral ratio technique on ambient vibrations. Measurements, processing and interpre-

tations. WP12 European commission - Research general directorate project no. EVG1-CT-2000-0026 SESAME. , *report D23*(December), 62 pp.

Bensen, G. D., Ritzwoller, M. H., Barmin, M. P., Levshin, A. L., Lin, F., Moschetti, M. P., ... Yang, Y. (2007). Processing seismic ambient noise data to obtain reliable broad-band surface wave dispersion measurements. *Geophysical Journal International*, *169*(3), 1239–1260. doi: 10.1111/j.1365-246X.2007.03374.x

Berg, E. M., Lin, F. C., Allam, A., Qiu, H., Shen, W., & Ben-Zion, Y. (2018). Tomography of Southern California Via Bayesian Joint Inversion of Rayleigh Wave Ellipticity and Phase Velocity From Ambient Noise Cross-Correlations. *Journal of Geophysical Research: Solid Earth*, *123*(11), 9933–9949. Retrieved from `https://doi.org/10.1029/2018JB016269` doi: 10.1029/2018JB016269

Boaga, J., Cassiani, G., Strobbia, C. L., & Vignoli, G. (2013). Mode misidentification in Rayleigh waves: Ellipticity as a cause and a cure. *Geophysics*, *78*(4). doi: 10.1190/GEO2012-0194.1

Bonnefoy-Claudet, S., Cotton, F., & Bard, P. Y. (2006). The nature of noise wavefield and its applications for site effects studies. A literature review. *Earth-Science Reviews*, *79*(3-4), 205–227. doi: 10.1016/j.earscirev.2006.07.004

Brenguier, F., Boué, P., Ben-Zion, Y., Vernon, F., Johnson, C. W., Mordret, A., ... Lecocq, T. (2019). Train Traffic as a Powerful Noise Source for Monitoring Active Faults With Seismic Interferometry. *Geophysical Research Letters*, *46*(16), 9529–9536. doi: 10.1029/2019GL083438

Fäh, D., Stamm, G., & Havenith, H. B. (2008). Analysis of three-component ambient vibration array measurements. *Geophysical Journal International*, *172*(1), 199–213. doi: 10.1111/j.1365-246X.2007.03625.x

Finger, C., Harrington, R., & Reinsch, T. (2022). The ZB Seismic Network, 2021–2022. *GFZ Data Services*. doi: doi:10.14470/MO7576467356

Finger, C., & Löer, K. (2023). *B3AMpy: Beamforming Toolbox for three-component ambient seismic noise.* doi: http://dx.doi.org/10.24406/fordatis/306

Finger, C., Roth, M. P., Dietl, M., Gotowik, A., Engels, N., Harrington, R. M., ... Saenger, E. H. (2023). The Weisweiler passive seismological network: optimised for state-of-the-art location and imaging methods. *Earth System Science Data*, *15*(6), 2655–2666. doi: 10.5194/essd-15-2655-2023

Finger, C., & Saenger, E. (2023). *Synthetic ambient seismic noise dataset for testing ambient-noise methods.* doi: http://dx.doi.org/10.24406/fordatis/302

Fritschle, T., Strozyk, F., Oswald, T., Stubbe, H., & Salamon, M. (2021). Deep geothermal energy potential at weisweiler, germany: Exploring subsurface mid-palaeozoic carbonate reservoir rocks. *Zeitschrift der Deutschen Gesellschaft fur Geowissenschaften*, *172*(3), 325–338. doi: 10.1127/zdgg/2021/0292

Galetti, E., Curtis, A., Baptie, B., Jenkins, D., & Nicolson, H. (2017). Transdimensional Love-wave tomography of the British Isles and shear-velocity structure of the East Irish Sea Basin from ambient-noise interferometry. *Geophysical Journal International*, *208*(1), 36–58. doi: 10.1093/gji/ggw286

Gotowik, A. (2022). *Investigating shear velocity profiles and their correlation to local geology in the Lower Rhine Embayment, Germany* (Master Thesis). Ruhr-Universität Bochum.

Herrmann, R. B. (2013). Computer programs in seismology: An evolving tool for instruction and research. *Seismological Research Letters*, *84*(6), 1081–1088. doi: 10.1785/0220110096

Lin, F. C., Schmandt, B., & Tsai, V. C. (2012). Joint inversion of Rayleigh wave phase velocity and ellipticity using USArray: Constraining velocity and density structure in the upper crust. *Geophysical Research Letters*, *39*(12), 1–7. doi: 10.1029/2012GL052196

Löer, K., & Finger, C. (2022). Mitigating array-induced bias in ambient noise beamforming. In *Egu general assembly* (pp. EGU22–3956). Retrieved from `https://doi.org/10.5194/egusphere-egu22-3956,2022` doi:

https://doi.org/10.5194/egusphere-egu22-3956,2022

Löer, K., Riahi, N., & Saenger, E. H. (2018). Three-component ambient noise beamforming in the Parkfield area. *Geophysical Journal International*.

Löer, K., Toledo, T., Norini, G., Zhang, X., Curtis, A., & Saenger, E. H. (2020). Imaging the deep structures of the Los Humeros geothermal field, Mexico, using three-component ambient noise beamforming. *Seismological Research Letters*.

Pankow, K. (2016). *FORGE nodal array 1 [Dataset].* International Federation of Digital Seismograph. doi: 10.7914/SN/8J_2016

Picozzi, M., Parolai, S., & Richwalski, S. M. (2005). Joint inversion of H/V ratios and dispersion curves from seismic noise: Estimating the S-wave velocity of bedrock. *Geophysical Research Letters*, *32*(11), 1–4. doi: 10.1029/2005GL022878

Podgorney, R. (2020). *Utah FORGE: Earth Model Mesh Data for Selected Surfaces.* Retrieved from `https://gdr.openei.org/submissions/1107`

Saenger, E. H., Gold, N., & Shapiro, S. A. (2000). Modeling the propagation of elastic waves using a modified finite-difference grid. *Wave Motion*, *31*(1), 77–92. doi: 10.1016/S0165-2125(99)00023-2

Scherbaum, F., Hinzen, K. G., & Ohrnberger, M. (2003). Determination of shallow shear wave velocity profiles in the cologne, Germany area using ambient vibrations. *Geophysical Journal International*, *152*(3), 597–612. doi: 10.1046/j.1365-246X.2003.01856.x

Toledo, T. (2020). Local Earthquake tomography of the Los Humeros geothermal field. *in preparation*.

Tuan, T. T., Scherbaum, F., & Malischewsky, P. G. (2011). On the relationship of peaks and troughs of the ellipticity (H/V) of Rayleigh waves and the transmission response of single layer over half-space models. *Geophysical Journal International*, *184*(2), 793–800. doi: 10.1111/j.1365-246X.2010.04863.x

Wathelet, M., Jongmans, D., Ohrnberger, M., & Bonnefoy-Claudet, S. (2008). Array performances for ambient vibrations on a shallow structure and consequences over Vs inversion. *Journal of Seismology*, *12*(1), 1–19. doi: 10.1007/s10950-007-9067-x

Wells, D., Lin, F., Pankow, K., Baker, B., & Bartley, J. (2022). Combining Dense Seismic Arrays and Broadband Data to Image the Subsurface Velocity Structure in Geothermally Active South-Central Utah. *Journal of Geophysical Research: Solid Earth*, 1–42. doi: 10.1029/2022jb024070

Zhang, W., & Gao, J. (2021). Model parameterizations in the time-domain multi-parameter acoustic least-squares reverse time migration. *Acta Geophysica*(0123456789). doi: 10.1007/s11600-021-00540-6

Depth of Sudden Velocity Changes derived from Multi-Mode Rayleigh Waves

C. Finger[1] and K. Löer[2]

[1]Fraunhofer IEG, Fraunhofer Institution for Energy Infrastructures and Geothermal Systems
[2]School of Geosciences , University of Aberdeen, now: Department of Geoscience & Engineering TU Delft

Key Points:

- We estimate the depth of sudden velocity increases from phase velocity and ellipticity of ambient-noise multi-mode Rayleigh waves
- Three-component ambient-noise beamforming is used to estimate phase velocity and ellipticity
- Feasibility is demonstrated with noise recordings from multiple sites and validated with results from other studies.

Corresponding author: Claudia Finger, `claudia.finger@ieg.fraunhofer.de`

Abstract

To integrate structural subsurface models and smooth seismic velocity models, they need to share common features and resolutions. Here, we propose a new approach for estimating the depth of sudden velocity changes from ambient-noise multi-mode Rayleigh waves applicable to a wide range of frequencies. Approximating the size and shape of the so-called energy ellipse at frequencies where the ellipticity has an extremum allows us to derive the depth of sudden velocity changes as the half height of the energy ellipse. We test our approach theoretically, numerically, and on real data from two geothermal sites by extracting Rayleigh wave ellipticities and phase velocities from three-component beamforming of ambient noise using the python code package B3AMpy. For a small-scale array, our approach validates the depth of quaternary sediments predicted by geological models. For deeper velocity changes, high uncertainties remain but the general trend of inclining boundaries can be recovered well. We demonstrate that, if impedance contrasts are larger than three, our approach is valid for multiple layers, laterally heterogeneous models, and a wide range of Poisson ratios.

Plain Language Summary

To effectively combine structural models and seismic velocity models, we've developed a new method. It estimates the depth of sudden changes in seismic velocity using Rayleigh waves from ambient noise. By analyzing extreme points in Rayleigh wave ellipticity, we determine the depth from the observed phase velocity at that point. We tested the method and found it works well for various scenarios, including multiple layers, heterogeneous models, and different material properties.

1 Introduction

Accurate representations of the subsurface are crucial for exploring natural resources, such as geothermal or hydrocarbon reservoirs, and estimating associated risks. Subsurface geophysical models can be structural, i.e., containing locations of faults and discontinuities, or represent a smooth spatial distribution of properties, i.e., as in seismic velocity models. Information from both types of models are crucial for estimating reservoir extends, and hence their economic viability, and accurately locating (micro-) seismicity to estimate and monitor the seismic hazard. Thus, structural and velocity models should ultimately be integrated into a common subsurface model that simultaneously includes smooth variations and sudden changes of elastic properties.

Active seismic surveys are widely used to obtain high-resolution structural models but are challenged by high costs and permitting issues, especially in urban areas. Earthquake tomographies can be used to constrain seismic velocities between hypocenters and seismic stations but require an adequate distribution of local seismic events to fully illuminate the subsurface (Toledo, 2020). Ambient seismic noise methods can image the subsurface regardless of the local seismicity level and without the need for active seismic sources. Although body waves have recently been identified in ambient noise recordings (Brenguier et al., 2019), most studies invert velocity profiles from surface wave dispersion curves (Löer et al., 2020; Galetti et al., 2017). However, the large wavelengths of low-frequency surface waves increase uncertainties at greater depths and result in smooth and gradient-like velocity models that lack sharp features. Thus, integration of active and passive methods is challenging due to different geometries, different frequencies, and a lack in common features to validate the integration. In this study, we aim to close the gap between active and passive subsurface models by retrieving structural information, i.e., the depth of major sudden velocity changes, from ambient noise Rayleigh waves. In contrast to other methods, such as horizontal-to-vertical spectral ratios (HVSR, (Bonnefoy-Claudet et al., 2006)), our approach does not rely on velocity information from secondary

studies and does not make prior assumptions about the wave types in seismic recordings. No inversion is needed to determine a preliminary depth estimate using our approach.

Several studies jointly inverted Rayleigh wave phase velocities and ellipticities for shallow (Picozzi et al., 2005) and deep (Berg et al., 2018) velocity models. If Rayleigh waves dominate the analysed frequency range, the horizontal-to-vertical spectral ratio (HVSR) curve closely resembles Rayleigh wave ellipticities (Fäh et al., 2008). The peak frequency of HVSR together with an estimate of the average shear velocity of the sediments can be used to estimate the thickness of sediments overlaying a stiffer bedrock, if the impedance contrast is larger than three (Bonnefoy-Claudet et al., 2006; Bard & Team, 2004). However, the accuracy of the depth estimate of HVSR strongly relies on accurate estimates of the shear-wave velocity. Since HVSR is typically applied to short recordings from single surface stations, sensitivity is in practice often limited to frequency ranges above 0.1 Hz and, thus, is limited to depths of about one hundred meters. It is assumed that the subsurface can be represented with a one-dimensional velocity profile. HVSR applied to single station recordings and to ambient-noise cross-correlations (Berg et al., 2018; Lin et al., 2012) are challenged by misidentifying wave types and modes. Thus, there is a need for a method that does not inherently assume the dominance of Rayleigh waves and works in a larger frequency range to image larger depth ranges.

In this study, we propose a new relation to estimate the depth of sudden velocity changes whenever phase velocity and ellipticity can be resolved over the same frequency range. We observe that Rayleigh wave ellipticities together with their phase velocities at particular frequencies can be used to estimate the depth of a velocity increase. The relationship we found seems to describe what we call an *energy ellipse* whose half height coincides with the depth of the velocity change. We validate the proposed approach using analytical approximations and a variety of one-dimensional velocity models. Three-component (3C) ambient noise beamforming at multiple seismic stations provides phase velocity and ellipticity of retrograde and prograde Rayleigh waves. We use the python code package B3AMpy (Finger & Löer, 2023; Löer & Finger, 2022) to perform 3C beamforming. The depth sensitivity depends mainly on the array geometry. We demonstrate the application of our new approach by applying 3C beamforming to synthetic waveforms and recorded waveforms from three seismic arrays at two sites. We find good agreements between our depth estimates and available depth estimates from active surveys and geological models. The accuracy of our new approach is comparable to HVSR results assuming the shear-wave velocity is perfectly known but is applicable to a wider depth range without prior assumptions or input from secondary studies.

2 Estimating the depth of sudden velocity changes using Rayleigh waves

Rayleigh waves propagating along the Earth's surface can be described with their direction of propagation (backazimuth ϕ), their frequency f, their horizontal propagation velocity (phase velocity v_{ph}) and their ellipticity e, that is the ratio of horizontal to vertical motion. The phase velocity v_{ph} is slightly smaller than the shear wave velocity v_s of the propagation medium (Aki & Richards, 1980). Ellipticity e mainly depends on the ratio of compressional wave speed to shear wave speed $\frac{v_p}{v_s}$ (Tuan et al., 2011) and is described as the ratio of horizontal to vertical particle motion $e = \frac{H}{V}$ (e.g., Herrmann, 2013). Both v_{ph} and e are frequency-dependent in non-homogeneous media and strongly influenced by step-wise velocity increases with depth (Boaga et al., 2013).

In homogeneous Poisson media, Rayleigh wave motion is elliptical and retrograde at the surface and inverts to prograde motion at greater depths. A particle at the surface is displaced in vertical and horizontal direction with peak motions shifted in phase by $\frac{\pi}{2}$ and with particle velocities in the nm to mm range. $e = \frac{H}{V}$ is smaller than one in homogeneous Poisson solids. The energy of a passing Rayleigh wave induces the displacement of all particles in a subvolume, which describes an elliptical motion visible in

the two-dimensional snapshots of the displacement wavefield (Figure 1 a and b). We refer to this as the energy ellipse. The size and shape of this energy ellipse can be calculated using the horizontal propagation velocity, i.e., the phase velocity v_{ph}, and frequency f of the Rayleigh wave as shown in the following. Both the ellipse of the particle motion at the surface and the energy ellipse have the same ellipticity e.

The wavelength $\lambda_R = \frac{v_{ph}}{f}$ of Rayleigh waves can be understood as the circumference of the energy ellipse, approximated as $C_e = \pi\sqrt{2(r_v^2 + r_h^2)}$, with r_v and r_h being the length of the major and minor half-axis of the ellipse. For both vertical and horizontal ellipses (Figure 1) r_v is the vertical half axis and $e = \frac{r_h}{r_v}$. An auxiliary circle with circumference C_e has a radius $r_v^{'} = \frac{C_e}{2\pi}$ (orange circles in Figure 1c). The difference between r_v of the ellipse and $r_v^{'}$ of the circle is the factor $\sqrt{\frac{2}{1+e^2}}$ representing the difference between circle and ellipse. $r_v^{'}$ is smaller than r_v if $e < 1$ and vice versa for $e > 1$ (Figure 1c). In practice, e is not well resolved over broad frequency ranges. Thus, assuming $r_v \approx r_v^{'}$, we can use the auxiliary circle to calculate the half-height of the energy ellipse r_v without explicitly using e:

$$r_v = \frac{v_{ph}}{2\pi f}, \tag{1}$$

with v_{ph} being the tangential velocity $v_t = r\omega$ at each point on the auxiliary circle and $\omega = 2\pi f$ being the angular velocity. Using $e = \frac{r_h}{r_v}$, we can estimate the half width of the energy ellipse as

$$r_h = r_v e = \frac{v_{ph} e}{2\pi f}. \tag{2}$$

For one-dimensional velocity profiles, v_{ph} and e can be estimated using Computer Programs in Seismology (CPS) (Herrmann, 2013). For a two-layer velocity model with a sudden velocity increase in a depth of $d = 1\,\mathrm{km}$ and $\frac{v_p}{v_s} = \sqrt{3}$ (Figure 2a), v_{ph} and $e = \frac{H}{V}$ are shown in Figure 2 b and c, respectively. The fundamental mode (superscript 0) and the first higher mode (superscript 1) are shown. Using equations 1 and 2, the size of the energy ellipse can be calculated (Figure 2d). The empirical relation $d_{HVSR} = \frac{v_s^1}{4 f_p^0}$ typically used to estimate the depth of sudden velocity changes in HVSR studies (Bonnefoy-Claudet et al., 2006)is plotted for comparison using the true shear-wave velocity v_s^1 given in the analytical model (Figure 2a).

At high frequencies, the fundamental mode (mode 0) is polarised vertically ($\frac{H}{V} < 1$) and both radii are smaller than the depth of the sudden velocity increase, $r_v > r_h << d$ (Figure 2d). With decreasing frequency, the radii increase with different rates until they have equal length, $r_h = r_v, e = 1$, here at $f_e^0 = f_p^1 = 0.57\,\mathrm{Hz}$, where f_e^0 is the frequency where the fundamental mode Rayleigh wave has an ellipticity of one and f_p^1 is the frequency where the first higher mode has a minimum in ellipticity. The deeper part of the Rayleigh wave already 'sees' the higher velocities at greater depths which causes different growth rates for r_v and r_h. For lower frequencies, $f < f_e^0$, one radius is larger than the depth of the velocity increase and the other is smaller than the depth of the velocity increase. If the shear velocity of the bottom layer is larger than the compressional velocity of the top layer, the ellipse changes to being horizontally polarised, $r_v < r_h$ (cf. Figure 1c right horizontal ellipse). Note that r_v and r_h are still calculated using v_{ph} (equations 1 and 2) but the ellipticity is now larger than one, $e > 1$, resulting in $r_h > r_v$. The two radii then increase at different rates for decreasing frequencies until r_v is equal to the depth of the sudden velocity increase, $r_v = d$ (Figure 2d). At this frequency, here at $f_p^0 = 0.43\,\mathrm{Hz}$, where e of the fundamental mode has reached its maximum, r_v is about equal to the depth of the sudden velocity increase. At even smaller frequencies, the radius of the second circle is larger than d and 'sees' the bottom layer velocities as well. e is declining again until the sensitivity of the energy ellipse is mostly to the deeper layer.

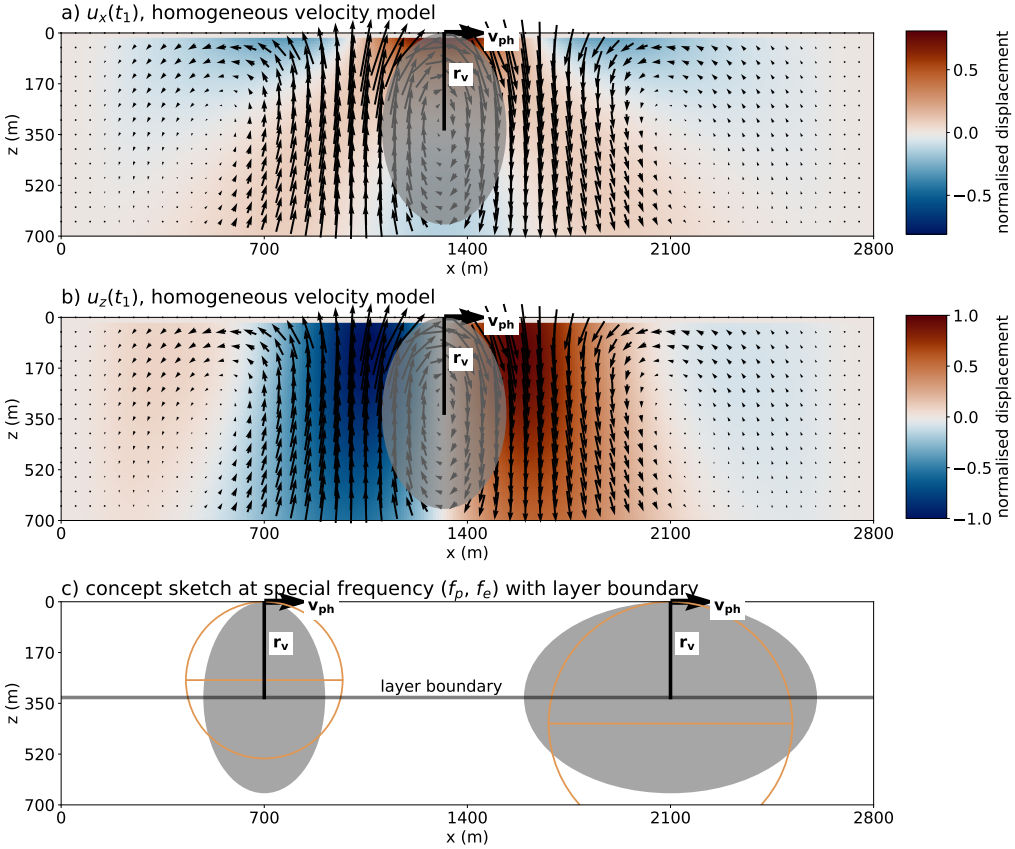

Figure 1. Snapshots of displacement in a) x direction and b) z direction for Rayleigh wave propagating in a homogeneous velocity model. Snapshots were created with a rotated staggered-grid finite difference scheme (Saenger et al., 2000). Energy ellipse is shaded grey. c) Sketch illustrating the estimation of the depth of a layer boundary as the half height of ellipse using the auxiliary circle (orange).

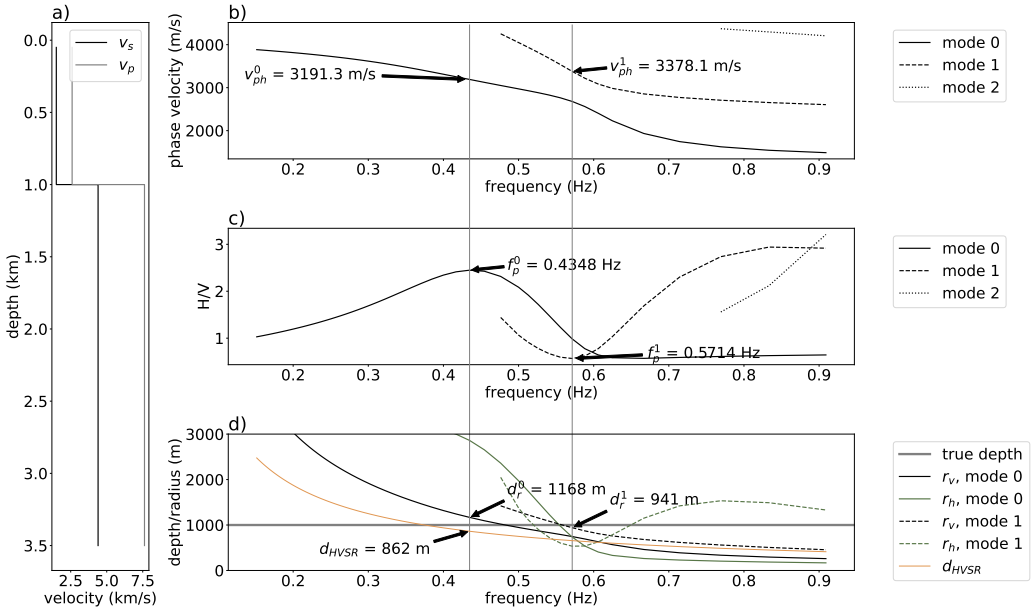

Figure 2. a) Input one-dimensional velocity model for analytical approximation of multi-mode Rayleigh wave b) phase velocity v_{ph} and c) ellipticity $e = \frac{H}{V}$ using (Herrmann, 2013). d) r_h and r_v calculated from b) and c) using equations 1 and 2. The empirical relation $d_{HVSR} = \frac{v_s^1}{4f_p}$, typically used in HVSR studies is plotted for comparison. Horizontal grey lines show frequencies where the fundamental and first higher mode experience extrema in ellipticity.

For the first higher mode (mode 1), a similar change can be observed (Figure 2d). The first higher mode is horizontally polarised for high frequencies with r_h being larger than the depth of the interface and r_v being smaller. With decreasing frequencies, r_v becomes as large as the depth of the sudden velocity increase with e being minimal, here at $f_p^1 = 0.57\,\text{Hz}$. Thus, we can also infer d from the first higher mode Rayleigh wave using equation 1 and the frequency f_p^1 where e of the first higher mode has a minimum. Note that in this case, the frequency where the fundamental mode Rayleigh wave is circular is equal to the frequency where the first higher mode has its minimum ellipticity ($f_p^1 = f_e^0$). Thus, this frequency can also be derived from the fundamental mode ellipticities which is beneficial since higher mode ellipticies are challenging to observe. However, for more complex velocity models, f_p^1 and f_e^0 may not coincide.

The depth estimates obtained from the fundamental and first higher mode are in this case $r_v^0(f_p^0) = 1168\,\text{m}$ and $r_v^1(f_p^1) = 941\,\text{m}$. Since the fundamental mode is horizontal at f_p^0 and the first higher mode is vertical at f_p^1 one value underestimates the depth and the other overestimates it (Figure 1c). The average depth estimate is, thus, 1054.5 m, a deviation of 5.5 % compared to the true depth. The depth estimate from the empirical relation typically used in horizontal-to-vertical spectral ratio (HVSR) studies (Bonnefoy-Claudet et al., 2006) is $d_{HVSR} = \frac{v_s^1}{4f_p^0} = \frac{1500\,\text{m/s]}}{4 \cdot 0.4348\,\text{Hz}} = 862\,\text{m}$, a deviation of more than 10 % based on the assumption that v_s^1 is known. Thus, our new approach is more accurate than HVSR in this case. Note that the depth estimate using the first higher mode is slightly more accurate than the one using the fundamental mode only.

Our proposed approach relies on the existence of horizontally polarised Rayleigh waves and works best if the first higher mode of Rayleigh waves exists at investigated frequencies. As described above, the fundamental Rayleigh wave becomes horizontally

polarised when the shear-wave velocity of the bottom layer is larger than the compressional-wave velocity of the shallower layer, $v_s^2 > v_p^1$. Assuming a poisson solid, i.e. $\frac{v_p}{v_s} = \sqrt{3}$, and densities of sandstone (about $\rho^1 = 2\,\mathrm{g/cm^3}$) and granite (about $\rho^2 = 2.63\,\mathrm{g/cm^3}$), the shear wave impedance contrast, $IC = \frac{rho^2 v_s^2}{rho^1 v_s^1}$ needs to be larger than 2.77 for v_s^2 to be larger than v_p^1. In our example velocity model (Figure 2) , the impedance contrast is four. For HVSR studies, a minimum impedance contrast of three is typically reported (Bonnefoy-Claudet et al., 2006). We tested different IC by changing v_s^2 (Figure 3a-d). For $IC = 2$ the first higher mode does not exist at lower frequencies and the peak in ellipticity of the fundamental mode is very small. Thus, the uncertainty of picking f_p^0 is high in this case and the deviation from the true source depth is high. We conclude that our method is valid for impedance contrasts larger than three. Note that only for $IC = 4$ is $r_v^1(f_p^1) = r_v^1(f_e^0)$ (Figure **??**d). An average from both modes would results in the most accurate depth estimate.

In the presence of fluids, the $\frac{v_p}{v_s}$-ratio can increase. Testing different $\frac{v_p}{v_s}$-ratios for both layers and using a constant impedance contrast of four reveals that with increasing $\frac{v_p}{v_s}$-ratio the phase velocities of the two modes become closer and mode mis-identification becomes more likely (Figure 3e). The frequency where the velocities of the two modes are closest together is very close to $f_e^0 = f_p^1$. This frequency is also referred to as the osculation frequency (Boaga et al., 2013). We can estimate the true depth of the sudden velocity increase relatively well for all tested $\frac{v_p}{v_s}$-ratios (Figure 3e-h). Note that also in these cases, the first higher mode provides more accurate depth estimates for a wider range of models than the fundamental mode and the depth estimate from HVSR (Figure 3h).

Adding an additional layer with varying impedance contrasts to the one-dimensional models reveals that the stronger impedance contrast tends to be retrieved. If the impedance contrasts of both velocity increases is the same, the depth estimate is closer to the deeper velocity increase (Figure 4). If the stronger impedance contrast is shallower (Figure 4e-h), the shallower layer boundary can be retrieved accurately using $r_v^1(f_e^0)$. If the stronger impedance contrast is deeper (Figure 4a-d), $r_v^1(f_e^0)$ retrieves the stronger shallower contrast if the impedance contrast is larger than three. Low velocity zones can occur and are thus an important consideration. Reducing the velocity of the middle layer (not shown), reveals that deviations from the true depth are higher but a rough estimate of the depth of the larger, in our case deeper, velocity increase is still possible.

3 Three-component ambient-noise beamforming of Rayleigh waves

To estimate the depth of sudden velocity increases using equation 1, we need to estimate v_{ph} and e over the desired frequency range. We choose Beamforming of three-component ambient noise (B3AM, (Löer & Finger, 2022)) for its distinct advantages of identifying wave types in small time windows of continuous waveforms and producing v_{ph} and e at the same discrete frequencies. Results from all processed time windows can be analysed statistically to obtain v_{ph} and e against frequency averaged over longer time windows. B3AM processes three-component waveforms recorded with multiple seismic stations and enables to identify prograde and retrograde Rayleigh waves separately, which allows a first indication of mode separation.

B3AM compares observed three-component phase shifts S^{3C} between stations of an array and between components of a station to theoretical phase shifts $a(k, \theta, \xi)$ created over a pre-defined grid of wavenumber k, backazimuth θ and polarisation parameters ξ. Backazimuth θ is defined as counter-clockwise from East. Polarisation parameters considered are the dip (inclination angle of body waves), the rotation around the x axis (i.e. for differentiating prograde and retrograde Rayleigh waves) and the ellipticity e^B defined in the range $[0, 2]$ with zero referring to a linear horizontal polarization, one referring to a circular polarisation and two referring to a linear vertical polarization.

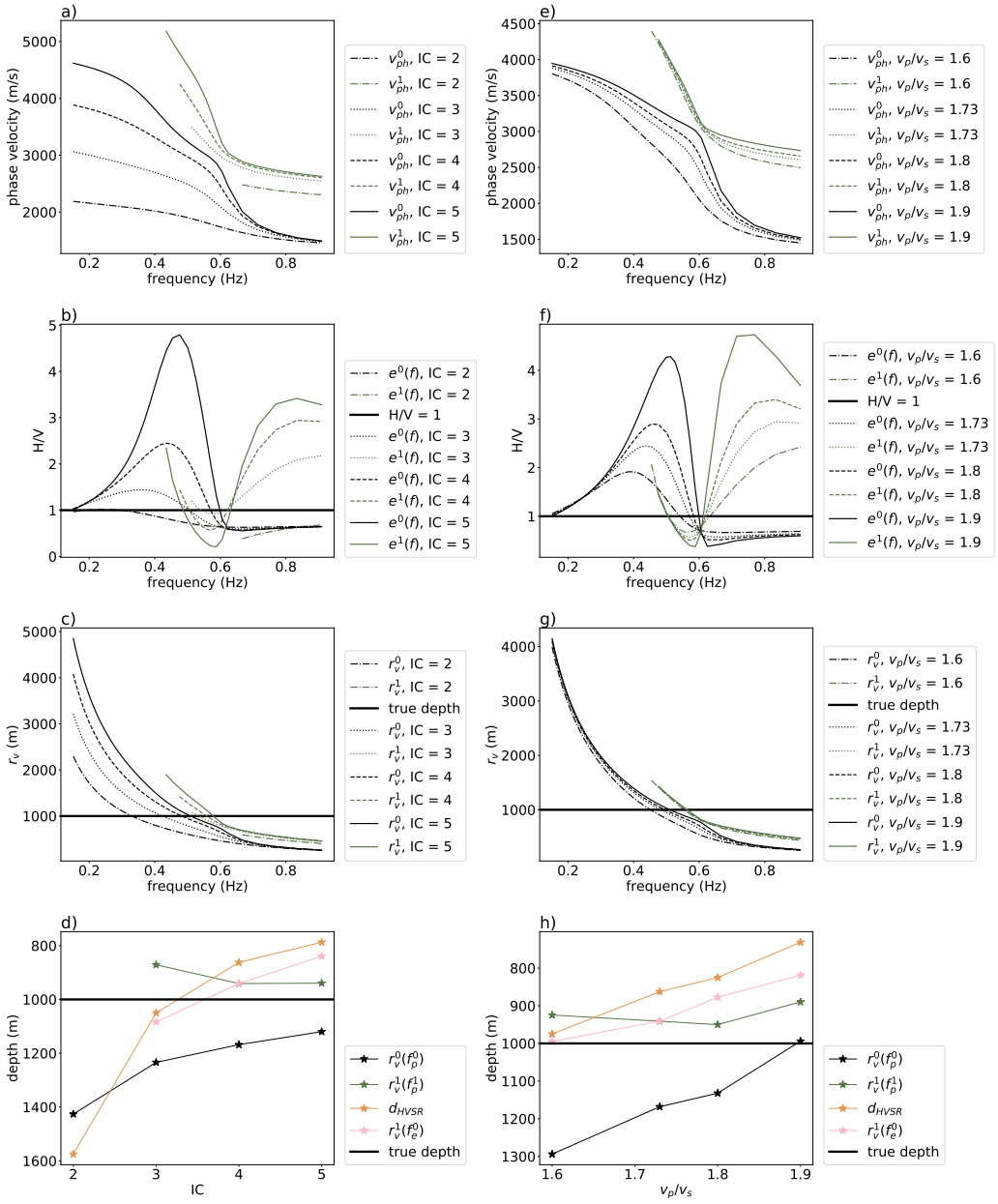

Figure 3. Phase velocity v_{ph}, H/V, r_v, and deviation to true depth for different types of theoretical velocity models. In a) to d) the impedance contrast IC between two layers is varied. In e) to h), the $\frac{v_p}{v_s}$-ratio is varied simultaneously for both layers and the impedance contrast is kept constant at $IC = 4$.

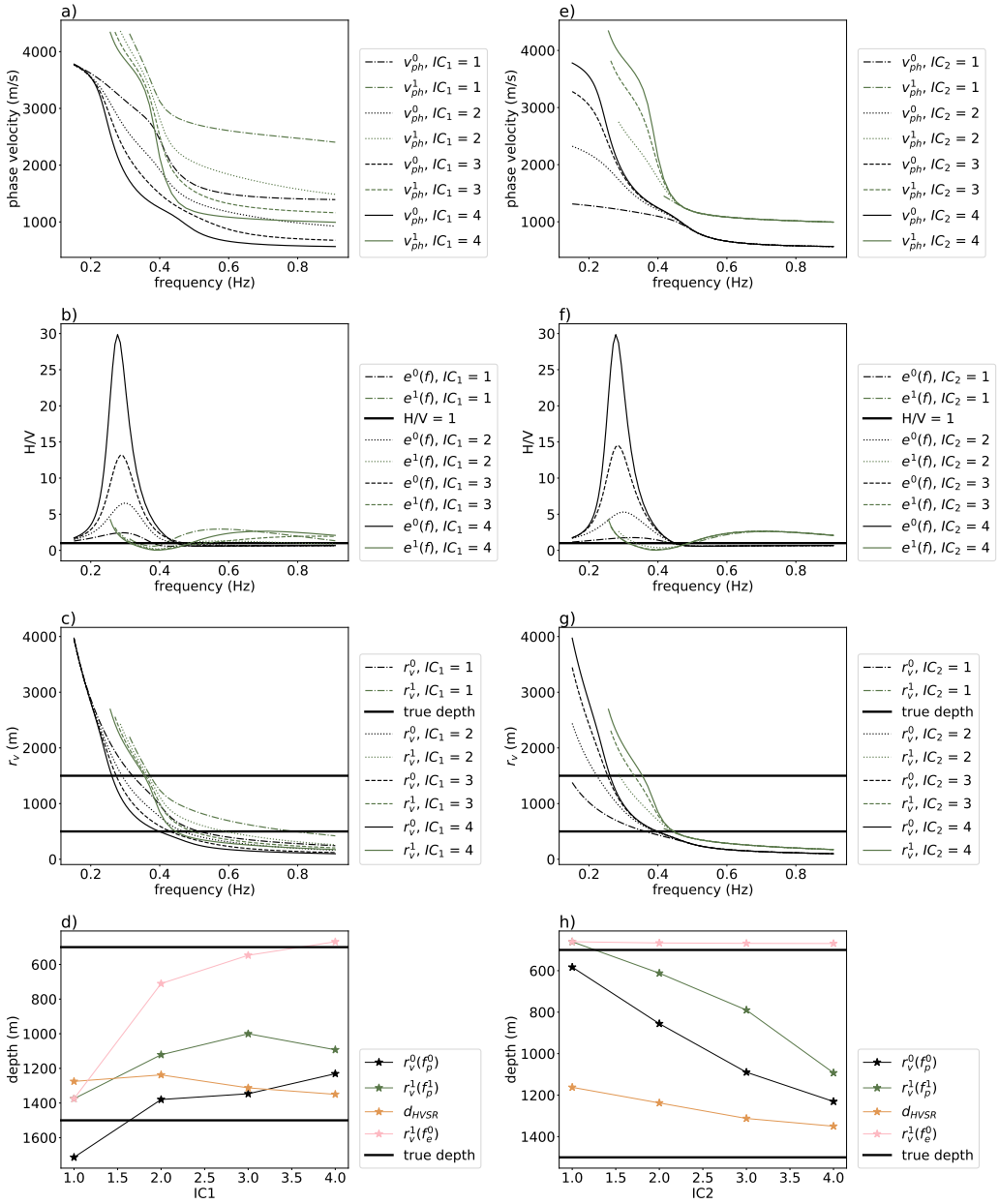

Figure 4. Phase velocity v_{ph}, H/V, r_v, and deviation to true depth for different types of theoretical velocity models. In a) to d), the impedance contrast of the shallower of two layer boundaries is varied while $\frac{v_p}{v_s} = 1.73$ and $IC = 4$. In e) to h), the impedance contrast of the deeper of the two layer boundaries is varied.

We can convert the ellipticity of B3AM to the more standardised definition using:

$$e = H/V = 2 - e^B, e^B \geq 1 \tag{3}$$

$$e = H/V = \frac{1}{e^B}, e^B \leq 1 \tag{4}$$

Further details about the used code can be found in (Löer & Finger, 2022).

Apart from detrending, demeaning and removal of instrument response, pre-processing should be kept to a minimum to avoid introducing artificial phase shifts. For the low frequency examples in this study (large station network in Wesweiler and station network in UtahFORGE), some pre-processing is required to obtain stable results for the low-frequency investigation. In these cases, we modify the running-mean time normalization proposed by (Bensen et al., 2007) to simultaneously weigh all three-component waveforms with the same weights calculated using one of the components. This is repeated with weights calculated over each component. Thus, relative amplitudes are always kept the same but spurious signals or earthquakes on each component are reduced in amplitude. No spectral whitening is applied to retain relative amplitudes between components and thus resolve ellipticities. Results from B3AM are normalised per frequency in post-processing to counteract unbalanced energy distributions across the frequencies.

As for all array methods, the wavenumber and frequency limits depend on the station geometry and subsurface velocities. We propose the following steps to determine the input parameters used to calculate the theoretical phase shifts in B3Am:

1. Plot the array response function (Löer et al., 2018) for multiple backazimuths and derive the minimum wavenumber k_{min} as the width of the central peak at half height and the maximum wavenumber k_{max} as the wavenumber where the first peak reaches half the height of the central peak as proposed by Wathelet et al. (2008). We consider k_{min} to represent the resolution limit, i.e. the smallest distinguishable wavenumbers, and use a wavenumber minimum of zero in B3AM to allow detection of vertical incident body waves. We found that using $k_{max}/2$ as the upper wavenumber limit works well in keeping the total number of discrete wavenumbers and, thus, the computation time low but obtaining high resolution in the well-resolved wavenumber parts.
2. Derive the desired wavenumber sampling Δk to achieve the desired depth sampling Δr. Since Δk and Δr are inversely related (equation 1), sampling of r_v is non-linear (Figure 5a). We recommend to severely oversample the wavenumber to artificially increase the radius sampling and reduce the wavenumber sampling through smoothing of the B3AM results in post-processing.
3. Make an educated guess about expected subsurface velocities (v_{min}, v_{max}) in the resolvable depth range estimated using k_{min} and k_{max} in equation 1.
4. Determine frequency range from wavenumber and velocity range. The minimum frequency $f_{min} = v_{max}k_{min}$ results from the highest expected velocity and the minimum resolvable wavenumber. The maximum frequency $f_{max} = v_{min}k_{max}$ results from the minimum expected frequency and the maximum resolvable wavenumber. Combining these limits defines the resolvable value range (Figure 5b).
5. Determine the desired frequency sampling and time window length for analyses based on the largest Period $T_{max} = \frac{1}{f_{min}}$. We use time window lengths of $4T_{max}$ and windows with 50 % overlap.

In this study, we sample e^B linearly with a spacing of 0.01. This results in equal weighting of horizontal and vertical Rayleigh waves but is different from e.g. HVSR curves where the horizontal part is usually sampled higher or exaggerated when plotting. The advantage of linearly sampling e^B is the ease of picking f_e^0. With our chosen e^B sampling, we can resolve H/V amplitudes from 0.01 to 100 with most precision for $H/V <$ 10.

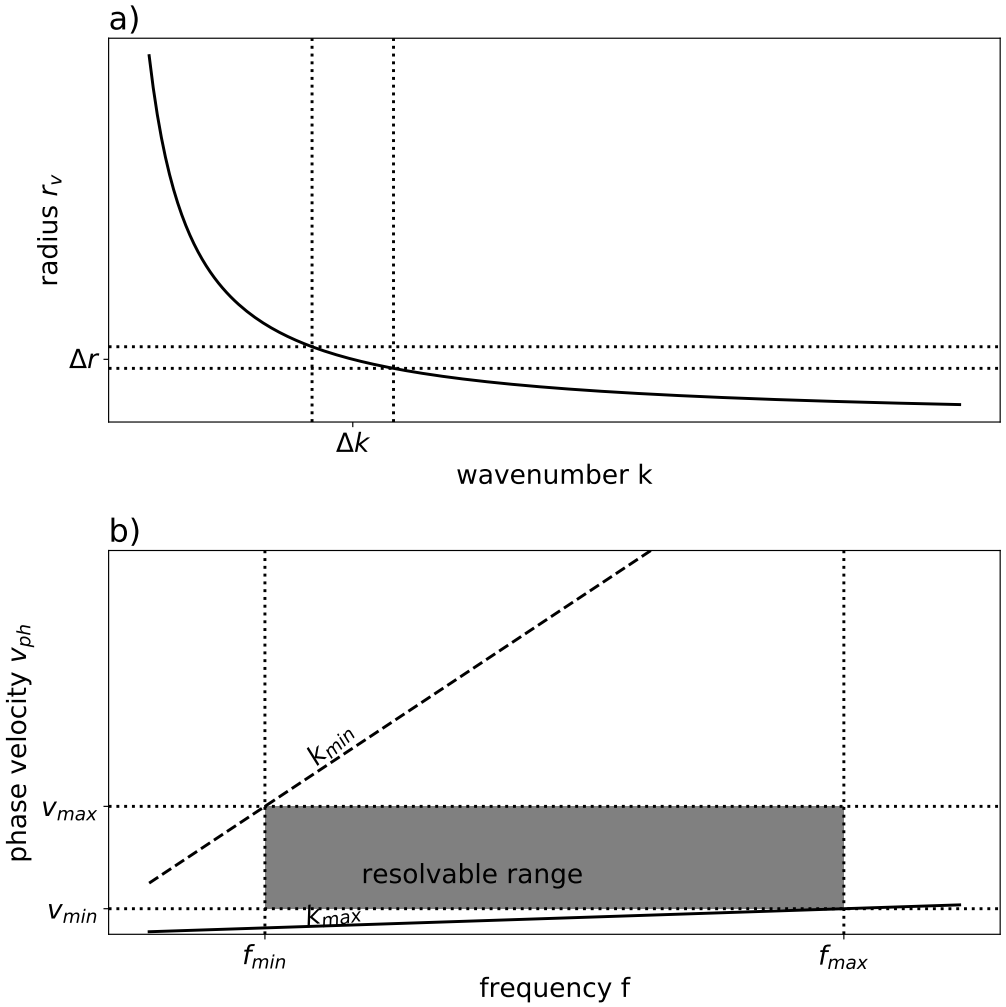

Figure 5. a) Relation between wavenumber sampling and radius r_v (equation 1). b) Relation between wavenumber, frequency and velocity limits and resolvable value range in B3AM.

B3AM provides wave type, polarisation parameters ξ and horizontal wavenumber k_h for every short time window per discrete frequency f. The propagation velocity for Rayleigh waves can be calculated as $v_{ph} = \frac{f}{k_h}$. B3AM results contain velocities outside the expected velocity range due to constant wavenumber sampling (Figure 5b). Thus, we manually exclude results with velocities smaller than v_{min} and larger than v_{max}. We then select only results identified by the polarization parameters as retrograde or prograde Rayleigh waves and calculate two-dimensional histograms of e^B and k_h over f. We smooth the histograms and pick the maximum per frequency and determine the uncertainty as the width of the local peak at half height. Some cases require manual correction of automatic picks which is indicated for the individual results. We calculate $r_v(f) = \frac{1}{2\pi k_h(f)}$ directly from the picked wavenumbers for all frequencies and pick f_p and f_e for all visible modes from the ellipticity curves. We determine the depth of velocity increases as $r_v(f_{p/e})$. Propagating relative errors from the wavenumber histograms to the depth estimates directly provides an uncertainty for our depth estimate.

4 Feasibility test using synthetic waveforms

To validate our approach in a realistic but controlled setting, we computed three-component full-waveform ambient seismic waveforms using a rotated staggered-grid finite-difference scheme (Saenger et al., 2000). The continuous waveforms recorded at the receiver positions described below are available from Finger and Saenger (2023).

The goal of the numerical simulations is a waveform dataset with similar characteristics as observed ambient seismic noise. The main attribute of ambient seismic noise is its seemingly random nature. Waves with different properties arrive from different directions at the receivers. To maximise this randomness, we implement 8000 randomly located point sources with a Ricker source time function with random origin times, random moment tensor components and random dominant frequencies. We insert these random sources in a three-dimensional velocity model. The inner part of the model, 2.5 times the aperture of the receiver array in the center of the model, is kept free from sources to adhere to the plane wave assumption inherent to the beamforming approach. Frequencies are limited between 0.01 Hz and 2 Hz to avoid numerical dispersion and stability issues. A total of $1540\,\mathrm{s} \approx 26 min$ of computed waveforms are generated.

The model size is 60 km by 60 km with a total depth of 30 km to allow large wavelengths to exist. The grid spacing is 50 m in all directions and the timestep is 0.005 s, which results in a realistic sampling rate of 200 Hz. The top of the model is a free surface and the sides and the bottom of the model are absorbing boundaries. 441 receivers are distributed in a regular grid of 21 by 21 receivers at the center of the model at the free surface. The inter-receiver distance is 500 m. We test two velocity models: a) the same velocity as in Figure 2 extended laterally to three dimensions and b) the same velocities as in Figure 2 but with a layer boundary dipping towards east.

4.1 Velocity model with two horizontal layers

We apply B3AM to the 26 minutes of synthetic waveform data recorded with the 100 center receivers and apply the workflow outlined in section 3 to obtain the maximum wavenumber limit as $\frac{k_{max}}{2} = 0.0001\,\mathrm{m}^{-1}$ and the wavenumber resolution as $\frac{k_{min}}{2} = 3.5{\cdot}10^{-5}\,\mathrm{m}^{-1}$. We oversample the wavenumber using 200 values. With expected velocities of $v_{min} = 1000\,\mathrm{m/s}$ to $v_{max} = 5000\,\mathrm{m/s}$, the analysed frequency range is $f_{min} = 0.2\,\mathrm{Hz}$ and $f_{max} = 1\,\mathrm{Hz}$. The time window length is 20.48 s resulting in 148 total analysed time windows. The frequency sampling is $\Delta f = 0.0244\,\mathrm{Hz}$ resulting in 32 analysed frequencies.

The two-dimensional smoothed histograms of $e^B(f)$ (Figure 6a and b) and $k_h(f)$ (Figure 6d and e) are used to pick multi-mode dispersion and ellipticity curves. The ret-

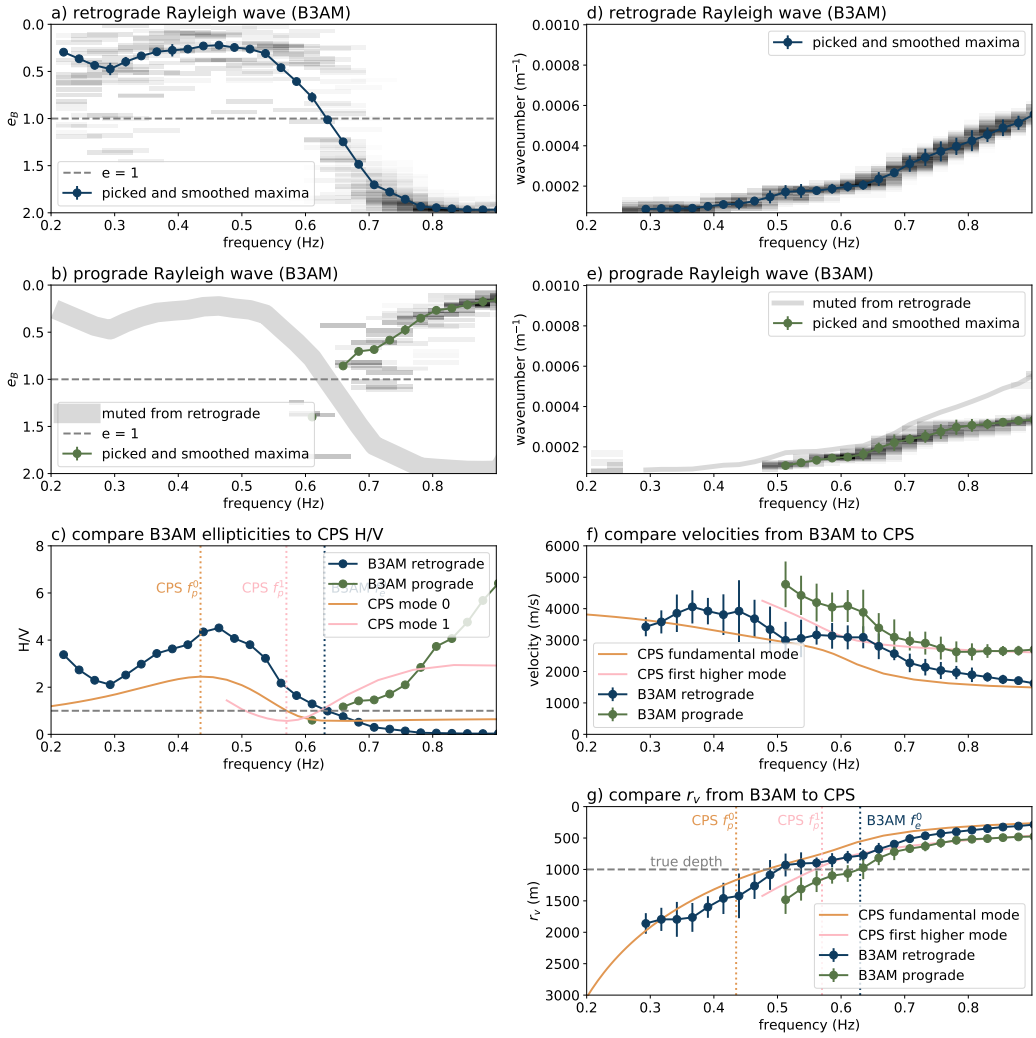

Figure 6. a) Histogram of $e^B(f)$ for retrograde Rayleigh waves from B3AM and picked and smoothed maxima. Uncertainties are too small to be visible. b) Histogram of $e^B(f)$ of prograde Rayleigh waves from B3AM and picked and smoothed maxima. c) Conversion of ellipticities to H/V and comparison to result from CPS. Vertical lines mark frequencies of extrema. d) Histogram of $k_h(f)$ of retrograde Rayleigh waves from B3AM and picked and smoothed maxima. e) Histogram of $k_h(f)$ of prograde Rayleigh waves from B3AM. f) Conversion from wavenumber to velocity and comparison to CPS. g) Half-height of Rayleigh wave energy ellipse r_v from B3AM and CPS results. Vertical lines show frequencies from c. Horizontal line shows true depth.

rograde ellipticities and wavenumbers can be picked unambiguously. The prograde ellipticities and wavenumbers are picked once the retrograde picks are removed from the prograde histograms. There is some ambiguity between retrograde and prograde waves. However, picked results from B3AM correspond relatively well to those from CPS (Figure 6c and f). As expected, the fundamental mode is retrograde and the first higher mode is prograde. Discrepancies in absolute values between B3AM results of the synthetic data and CPS results could stem from uncertainties of the approaches but do not alter the final depth estimates. Picking $f_e^0 = 0.63\,\mathrm{Hz}$ from B3AM and estimating the depth of the sudden velocity change as $r_v^1(f_e^0)$ results in a depth estimate of $973.6\,\mathrm{m} \pm 356.1\,\mathrm{m}$, a deviation of less than 3% to the true depth.

4.2 Velocity model with inclined layer boundary

We apply B3AM to the 26 minutes of continuous synthetic waveform data created with the inclined-layer velocity model. We analyse 100 receivers at a time and then move all receivers one receiver over to analyse the next 100 receivers. In this manner, we analyse a total of 12 subsets of receivers. We use the same parameters for B3AM as for the previous case and estimate the depth of the velocity increase from $r_v^1(f_e^0)$, the half height of the prograde Rayleigh wave energy ellipse at f_e^0, the frequency where the retrograde Rayleigh wave is circular. We find a good agreement of true and estimated depth across all subarrays (Figure 7) with deviations of less than 10% for half of the subarrays. B3AM seems to generally overestimate the depth in this case. Variations in depth estimate accuracy could result from uncertainty in picking. We only analysed 32 discrete frequencies. For some cases, differences between subarrays are smaller than the resolution. Additionally, the backazimuth of the Rayleigh waves could influence if the depth is under- or overestimated if the velocity model varies laterally. We investigated the prominent backazimuth for each subarray but could not find a clear correlation to the depth estimate deviation. The footprint of the array, here 4.5 km, does not seem to influence results and depth estimates sem to be an average over the footprint. Therefore, we conclude that the deviation stems mostly from the inherent uncertainties of the method.

5 Application to recorded ambient noise

We apply the developed workflow to two seismic station deployments. At the geothermal test site UtahFORGE in Utah, USA, reflection seismic data show a strong impedance contrast between sediments and the granitoid bedrock (Podgorney, 2020). We use this to validate our approach in a real world scenario. In Western Germany surrounding the town of Eschweiler-Weisweiler, no active seismic surveys have been performed and, thus, geological models (Fritschle et al., 2021) have large uncertainties. Our approach gives the first analysis into the deeper subsurface.

5.1 Application site UtahFORGE, USA

In December 2016, 49 Fairfield Nodal Zland three-component (3C) geophones were deployed in a regular grid with 600 m inter-station spacing at the geothermal site UtahFORGE in Utah, USA (Pankow, 2016). We analyse 48 hours of continuous waveform data on 20.12.2016 and 21.12.2016 using four subsets of 16 receivers each. We restricted the upper wavenumber limit to $k_{max} = 0.0004\,\mathrm{m}^{-1}$ and the frequency range from 0.05 Hz to 0.5 Hz for maximum sensitivity in the expected depth range. Raw waveforms are preprocessed with the modified moving average time normalisation as described in section 3 for more stable results. Ellipticities and wavenumbers showed large uncertainties that made picking challenging. We manually had to revise the automatic picks. The B3AM results for the first 16-receiver subset is shown in Figure 8.

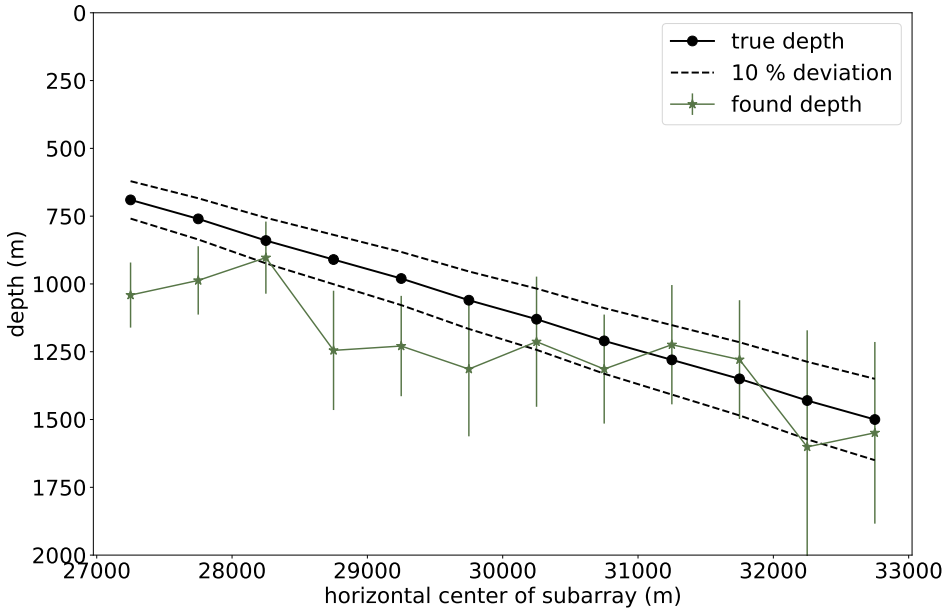

Figure 7. Estimated depth ($r_v^1(f_e^0)$) of sudden velocity increase derived using multiple subsets of receivers for the model with an inclined layer boundary.

Comparing the depth estimates from all four 16-receiver subsets to the depth of the granitoid boundary averaged in North-South direction as reported by (Podgorney, 2020) reveals that B3AM recovers the general trend of the inclined boundary well but overestimates the depth significantly. The lower limit of the uncertainty falls within the 50 % deviation. The regional velocity model derived from ambient-noise phase velocities and H/V ratios (Wells et al., 2022) reveals an extensive low velocity zone down to depths of about 2 km not taking the elevation into account. Assuming our approach is sensitive to this deeper velocity increase would mean that the deeper velocitiy increase is sharper than the sediment-to-granitoid boundary at shallower depths. Using estimated velocites from Zhang and Gao (2021) and typical densities for sandstone and granite, we estimate the shear impedance contrast of the sediment-to-granitoid interface to be $IC = \frac{2630\,\mathrm{kg/m^3}\,3000\,\mathrm{m/s}}{2000\,\mathrm{kg/m^3}2000\,\mathrm{m/s}} = 1.97$ and would, thus, be too small for our approach. Thus, we conclude that our approach may confirm a deeper increase in velocities.

5.2 Application site Weisweiler, Germany

Surrounding the town of Eschweiler-Weisweiler, in the western part of Germany, a small-scale short-term array has been deployed in June 2021 followed by a larger network consisting of among others 27 broadband seismic stations (Finger et al., 2023).

We analyse two hours of continuous waveform data recorded in the night of June 20th 2021 with the small-scale array with B3AM. The small array enables the analysis of wavenumbers up to $k_{max} = 0.023\,\mathrm{m}^{-1}$ in the frequency range of $f_{min} = 1\,\mathrm{Hz}$ to $f_{max} = 4.6\,\mathrm{Hz}$. B3AM results seem to be sensitive down to frequencies just above the peak frequency of HVSR curves (Figure 10c). This high-filtering effect has been observed in other studies as well (Scherbaum et al., 2003). Thus, the peak frequency of the fundamental mode cannot be resolved well in this case. However, f_e^0 can be clearly identified as 2.44 Hz.

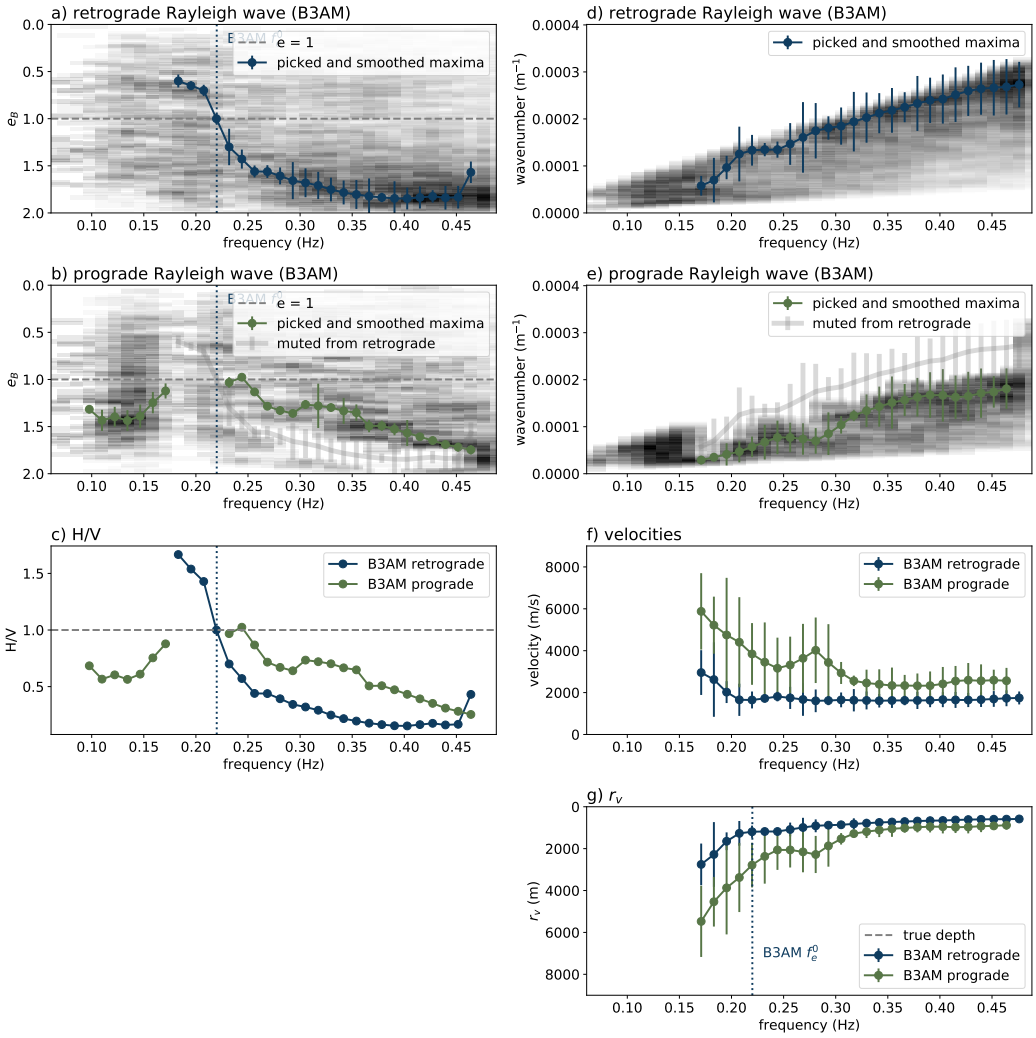

Figure 8. B3AM results of 48 hours of continuous data recorded with the first of four 16-receiver subsets of the Forge array. a) Ellipticities of retrograde Rayleigh wave, b) Ellipticities of prograde Rayleigh wave, c) Wavenumber of retrograde Rayleigh wave, d) Wavenumber of prograde Rayleigh wave. e) Half-height r_v of energy ellipse for retrograde and prograde Rayleigh wave.

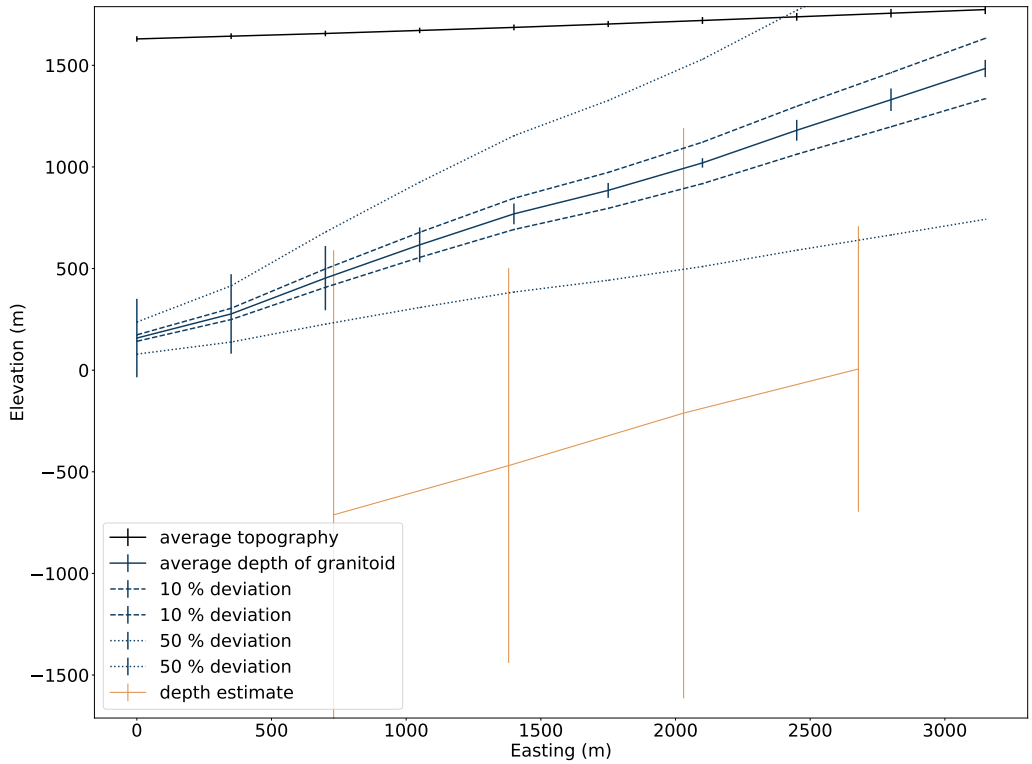

Figure 9. Depth estimates from all four 16-receiver subsets of the FORGE array compared to the topography and depth of the known granitoid boundary averaged in North-South direction.

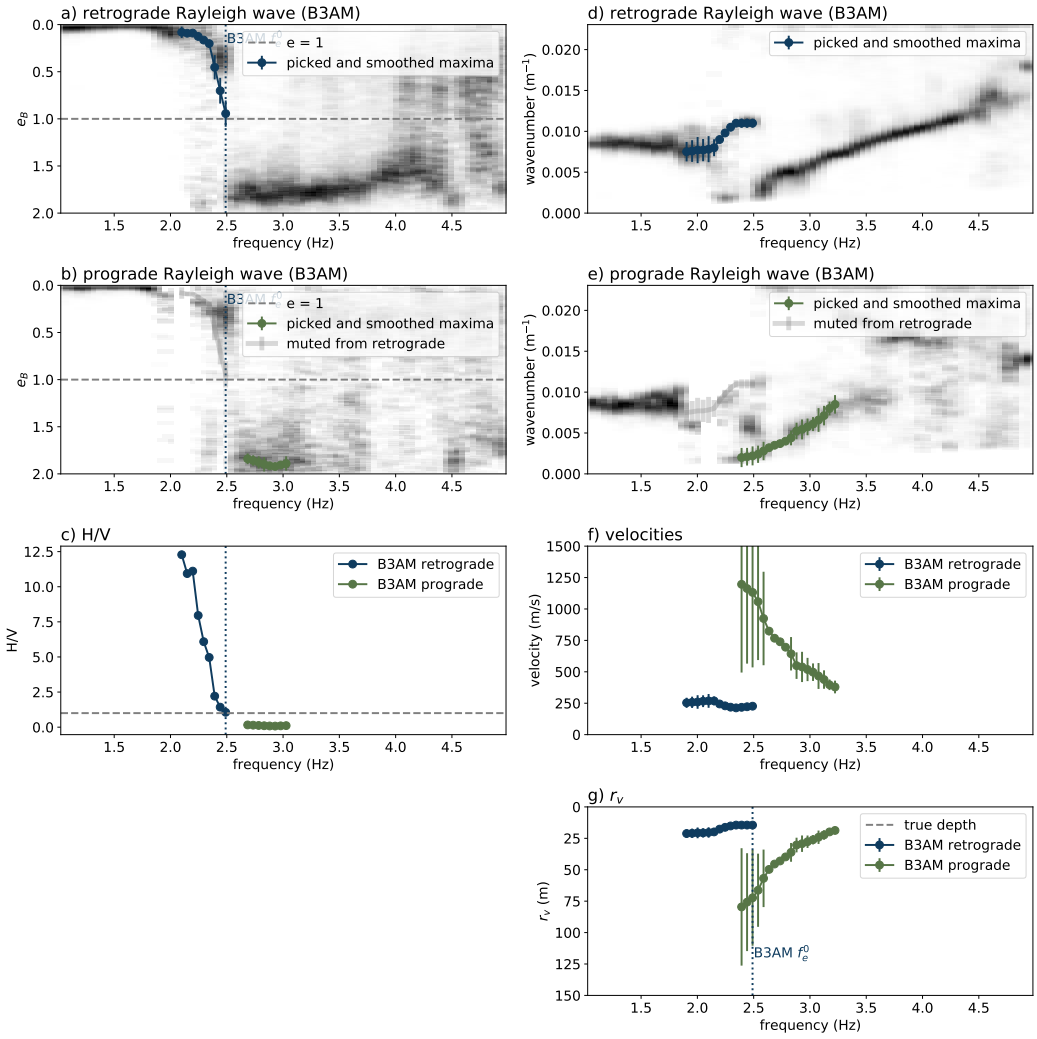

Figure 10. Results of retrograde and prograde Ralyeigh waves from B3AM for two hours of continuous noise data recorded with the seven stations of the small-scale network. Ellipticities of a) retrograde Rayleigh waves and b) prograde Rayleigh waves. Wavenumbers of c) retrograde and d) prograde Rayleigh waves. f) Half-height r_v of energy ellipse for retrograde and prograde Rayleigh waves. Vertical lines mark picked interesting frequencies in a - c used to estimate depth in f.

The prograde ellipticities have a minimum around 2.8 Hz. In the retrograde and prograde wavenumbers (Figure 10d and e), some mode leakage seems to occur. By manually picking modes in restricted frequency ranges allows to estimate the depth as $r_v^1(f_e^0 = 2.44\,\text{Hz}) = 72.3\,\text{m} \pm 29.9\,\text{m}$. This is in good agreement with geological models (Fritschle et al., 2021) that estimate a thickness of about 60 m for the quaternary sediments. Using the HVSR peak frequency of 1.6 Hz derived in Gotowik (2022) and the minimal shear velocity of 400 m/s estimated from our B3AM results, we get a depth estimate of $\frac{400\,\text{m/s}}{4 \cdot 1.6\,\text{Hz}} = 63\,\text{m}$ using the empirical HVSR equation.

For the large network in Weisweiler, we analyse 48 hours of continuous waveform data recorded at 23 of the broadband stations (Nanometrics Trillium 20s and 120s) that were recording with all components on 16.10.2021 and 17.10.2021. We use a maximum

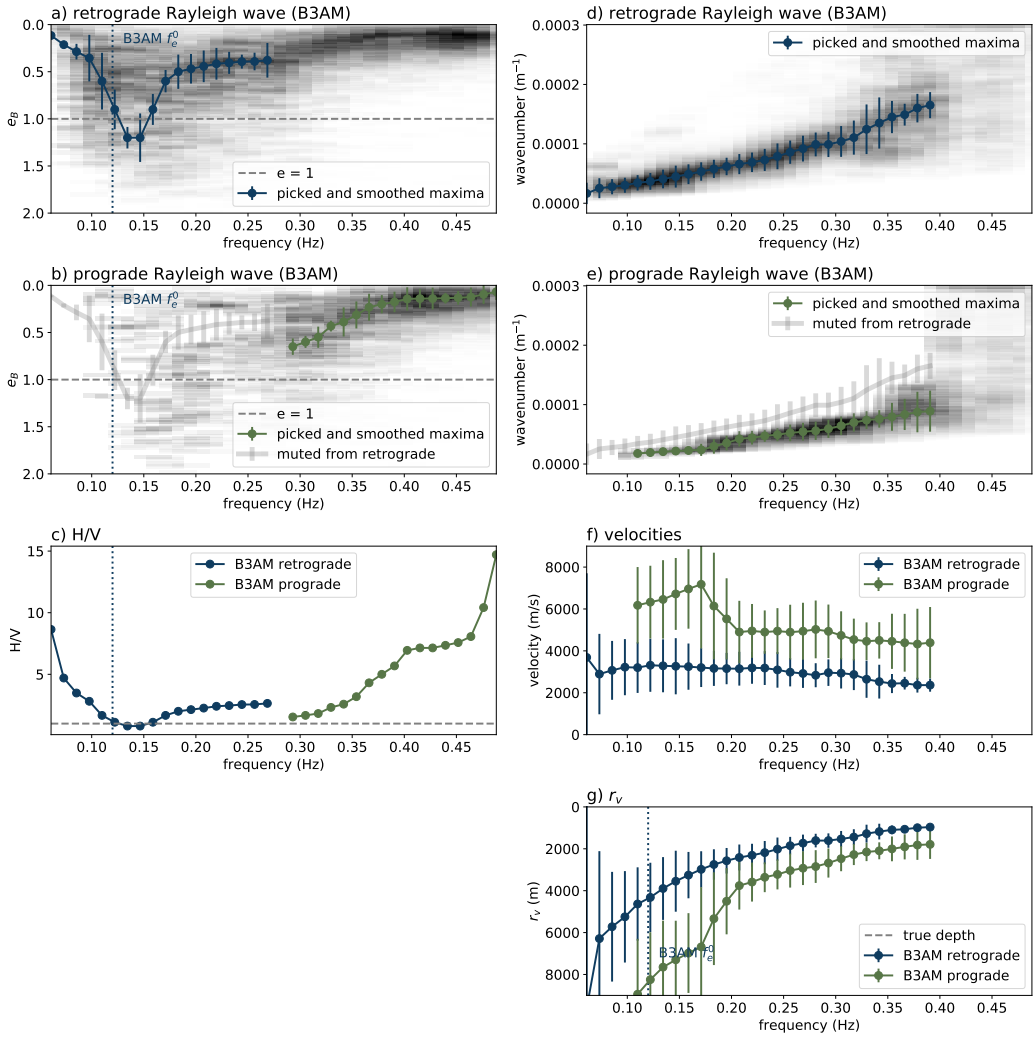

Figure 11. B3AM results of 48 hours of continuous data recorded with 23 stations of the large Weisweiler network. a) Ellipticities of retrograde Rayleigh wave, b) ellipticities of prograde Rayleigh wave, c) wavenumber of retrograde Rayleigh wave, d) wavenumber of prograde Rayleigh wave and e) half-height r_v of energy ellipse for retrograde and prograde Rayleigh wave.

wavenumber limit of $k_{max} = 0.0003\,\mathrm{m}^{-1}$. We analyse frequencies in the range of 0.05 Hz to 0.5 Hz and apply the modified running mean time normalization during pre-processing to get more stable results.

While wavenumbers are well-resolved (Figure 11d and e), ellipticities are not well resolved in this case (Figure 11a and b). Contrary to the simplified models in previous sections, mostly horizontal polarised ellipses seem to be found for the retrograde wave. However, at around 0.15 Hz the retrograde ellipticities seem to become vertical. If we assume that this is f_e^0, we can estimate a depth as $r_v^1(f_e^0)$ of more than 8 km (Figure 11e). This is deeper than any presently available models. The reported depth of the 'Massenkalk' in the geological models in (Fritschle et al., 2021) is about half of that depth. Alternatively assuming that the retrograde ellipticities represent the first higher mode in this case, we can pick $r_v^1(f_p^1) \approx 4\,\mathrm{km}$ but with high uncertainties. We tried to analyse subsets of receivers to observe lateral changes of this depth but uncertainties are too high

to make a robust estimate. Similarly as for the case in FORGE, we can conclude that shallower velocity changes have probably too small impedance contrasts for our approach. In this complex geological setting, our simplified approach to estimate the depth of sudden velocity changes might be too simplified to provide a robust estimate.

6 Discussion

We present here a new approach to derive the depth of sudden velocity changes from Rayleigh waves recorded at seismic station networks. If ellipticity and phase velocity of Rayleigh waves can be retrieved over the same frequency range, the depth can be estimated as the half height of the energy ellipse at the peak frequencies in ellipticity. This approach has been validated using analytical approximations for a multitude of velocity models. The depth can be estimated within reasonable uncertainties for impedance contrasts above three and different $\frac{v_p}{v_s}$-ratios. In all tested multi-layer models, the strongest impedance contrast is retrieved. This approach can be applied to any seismic recordings containing Rayleigh waves in the interesting frequency range. The prevalence of Rayleigh waves in ambient seismic noise is an advantage for statistically more stable results. In this study, we only applied it the method to surface observations but we can envision an application also to borehole stations with an adapted workflow.

We observe that wavenumbers can generally be better resolved than ellipticities using B3AM. This could be due to the assumption of perfect ellipses that are neither tilted nor distorted. This assumption does not hold true for lower frequencies sensitive to greater depths where velocities cannot be considered homogeneous anymore. Wavenumbers are resolved down to a frequency slightly above the peak frequency of fundamental mode ellipticities. This high-pass filtering effect caused by low-velocity layers overlaying high-velocity layers is a common phenomenon (Scherbaum et al., 2003). The large uncertainties in ellipticities, especially for lower frequencies, may be reduced by analysing more waveform data. Wavenumber uncertainty can be improved with denser station networks. Generally, uncertainties in depth estimates increase with decreasing frequency. With dense enough stations networks and high enough wavenumber sampling, these uncertainties are sufficiently small for an initial estimate of the depth of sudden velocity changes.

The ellipticity e_B in B3AM is linearly resolved between zero and two with higher resolution around $e_B = 1$. This enables the straight-forward identification of f_e^0. At this frequency, mode mis-identification is likely. Identifying f_e^0 thus helps in distinguishing modes and can alleviate some of the challenges in multi-mode dispersion curve analysis (Boaga et al., 2013). Calculating r_v additionally helps to understand the Rayleigh wave behaviour in complex velocity models and can give a first estimate of the depth of Rayleigh wave sensitivity. Our proposed approach benefits from multi-mode analysis of Rayleigh waves since depths are over- or underestimated depending on the orientation of the energy ellipse.

When velocity models are not strictly one dimensional, uncertainties can be high since waves arriving from different directions are influenced by different velocities. The resulting one-dimensional depth estimate is an average of velocities over the footprint of the array. The horizontal footprint of this method is a combination of the total used array size and the horizontal size r_h of the Rayleigh wave energy ellipse. We found that in the synthetic test cases, small lateral changes could be resolved by using overlapping subsets of receivers.

We see multiple possible uses of our proposed new relations:

- Determine osculation frequency (f_e^0) and, thus, aid in preventing mode misidentification when using Rayleigh wave dispersion curves.

- Estimate conversion from frequency to depth for Rayleigh wave phase and group velocity using r_v as an indicator for depth.
- Determine the depth of sudden high-impedance velocity changes for use as constraints in inversions of Rayleigh wave dispersion curves to constrain and validate geological models.
- Combine our approach with HVSR studies for increasing accuracy of shallow velocity structures.
- Use depth of sudden velocity changes to integrate passive and active seismic methods based on common (sub-) horizontal contrasts from both methods.

7 Conclusion

We present a new approach to estimate the depth of sudden velocity changes using seismic arrays that generally provides more accurate results than HVSR. Our approach is fully self-contained, i.e., no information from other studies needed, and does not rely on a priori assumptions about the wavefield. Approximation of the size of the energy ellipse enables a data-driven workflow for initial estimates of the depth of strong impedance contrasts. The capabilities of B3AM to identify and separate wave types from ambient-seismic noise recording enables multi-mode Rayleigh waves to be used in our approach and, thus, significantly increases the depth accuracy. We demonstrated the applicability at two sites in Utah, USA, and in Germany. While high uncertainties remain for the depth of deep velocity changes, this approach shows a high potential to increase accuracy of velocity models on multiple scales.

8 Open Research

The most recent version of the B3AM code for the python version used in this study can be downloaded from github (https://github.com/cl-finger/B3Ampy) with the version used in this study archived at Finger and Löer (2023). The numerical data created with the rotated staggered-grid finite difference code can be found at Finger and Saenger (2023). The nodal seismic data for Forge is available from (Pankow, 2016) and the depth of the granitoid boundary from (Podgorney, 2020). The passive seismic dataset recorded in Weisweiler, Germany can be obtained from (Finger et al., 2022). A detailed description of this dataset can be found in (Finger et al., 2023).

Acknowledgments

This project has been subsidized through the Cofund GEOTHERMICA, which is supported by the European Union's HORIZON 2020 programme for research, technological development and demonstration under grant agreement no. 731117 (DEEP). The german sub-project DEEP-SIGHT has been funded by the 'Bundesministerium für Wirtschaft und Klima' under project number 03EE4016. The authors gratefully acknowledge the Gauss Centre for Supercomputing e.V. (`http://www.gauss-centre.eu`, last access: 14 September 2023) for funding this project by providing computing time through the John von Neumann Institute for Computing (NIC) on the GCS Supercomputer JUWELS at Jülich Supercomputing Centre (JSC). We thank Erik H. Saenger for providing the finite-difference code HeidimodX.

References

Aki, K., & Richards, P. (1980). *Quantitative Seismology: Theory and Methods.* WH Freeman & Co.

Bard, P. Y., & Team. (2004). Guidelines for the implementation of the H/V spectral ratio technique on ambient vibrations. Measurements, processing and interpre-

tations. WP12 European commission - Research general directorate project no. EVG1-CT-2000-0026 SESAME. , *report D23*(December), 62 pp.

Bensen, G. D., Ritzwoller, M. H., Barmin, M. P., Levshin, A. L., Lin, F., Moschetti, M. P., ... Yang, Y. (2007). Processing seismic ambient noise data to obtain reliable broad-band surface wave dispersion measurements. *Geophysical Journal International*, *169*(3), 1239–1260. doi: 10.1111/j.1365-246X.2007.03374.x

Berg, E. M., Lin, F. C., Allam, A., Qiu, H., Shen, W., & Ben-Zion, Y. (2018). Tomography of Southern California Via Bayesian Joint Inversion of Rayleigh Wave Ellipticity and Phase Velocity From Ambient Noise Cross-Correlations. *Journal of Geophysical Research: Solid Earth*, *123*(11), 9933–9949. Retrieved from `https://doi.org/10.1029/2018JB016269` doi: 10.1029/2018JB016269

Boaga, J., Cassiani, G., Strobbia, C. L., & Vignoli, G. (2013). Mode misidentification in Rayleigh waves: Ellipticity as a cause and a cure. *Geophysics*, *78*(4). doi: 10.1190/GEO2012-0194.1

Bonnefoy-Claudet, S., Cotton, F., & Bard, P. Y. (2006). The nature of noise wavefield and its applications for site effects studies. A literature review. *Earth-Science Reviews*, *79*(3-4), 205–227. doi: 10.1016/j.earscirev.2006.07.004

Brenguier, F., Boué, P., Ben-Zion, Y., Vernon, F., Johnson, C. W., Mordret, A., ... Lecocq, T. (2019). Train Traffic as a Powerful Noise Source for Monitoring Active Faults With Seismic Interferometry. *Geophysical Research Letters*, *46*(16), 9529–9536. doi: 10.1029/2019GL083438

Fäh, D., Stamm, G., & Havenith, H. B. (2008). Analysis of three-component ambient vibration array measurements. *Geophysical Journal International*, *172*(1), 199–213. doi: 10.1111/j.1365-246X.2007.03625.x

Finger, C., Harrington, R., & Reinsch, T. (2022). The ZB Seismic Network, 2021–2022. *GFZ Data Services*. doi: doi:10.14470/MO7576467356

Finger, C., & Löer, K. (2023). *B3AMpy: Beamforming Toolbox for three-component ambient seismic noise.* doi: http://dx.doi.org/10.24406/fordatis/306

Finger, C., Roth, M. P., Dietl, M., Gotowik, A., Engels, N., Harrington, R. M., ... Saenger, E. H. (2023). The Weisweiler passive seismological network: optimised for state-of-the-art location and imaging methods. *Earth System Science Data*, *15*(6), 2655–2666. doi: 10.5194/essd-15-2655-2023

Finger, C., & Saenger, E. (2023). *Synthetic ambient seismic noise dataset for testing ambient-noise methods.* doi: http://dx.doi.org/10.24406/fordatis/302

Fritschle, T., Strozyk, F., Oswald, T., Stubbe, H., & Salamon, M. (2021). Deep geothermal energy potential at weisweiler, germany: Exploring subsurface mid-palaeozoic carbonate reservoir rocks. *Zeitschrift der Deutschen Gesellschaft fur Geowissenschaften*, *172*(3), 325–338. doi: 10.1127/zdgg/2021/0292

Galetti, E., Curtis, A., Baptie, B., Jenkins, D., & Nicolson, H. (2017). Transdimensional Love-wave tomography of the British Isles and shear-velocity structure of the East Irish Sea Basin from ambient-noise interferometry. *Geophysical Journal International*, *208*(1), 36–58. doi: 10.1093/gji/ggw286

Gotowik, A. (2022). *Investigating shear velocity profiles and their correlation to local geology in the Lower Rhine Embayment, Germany* (Master Thesis). Ruhr-Universität Bochum.

Herrmann, R. B. (2013). Computer programs in seismology: An evolving tool for instruction and research. *Seismological Research Letters*, *84*(6), 1081–1088. doi: 10.1785/0220110096

Lin, F. C., Schmandt, B., & Tsai, V. C. (2012). Joint inversion of Rayleigh wave phase velocity and ellipticity using USArray: Constraining velocity and density structure in the upper crust. *Geophysical Research Letters*, *39*(12), 1–7. doi: 10.1029/2012GL052196

Löer, K., & Finger, C. (2022). Mitigating array-induced bias in ambient noise beamforming. In *Egu general assembly* (pp. EGU22–3956). Retrieved from `https://doi.org/10.5194/egusphere-egu22-3956,2022` doi:

https://doi.org/10.5194/egusphere-egu22-3956,2022

Löer, K., Riahi, N., & Saenger, E. H. (2018). Three-component ambient noise beamforming in the Parkfield area. *Geophysical Journal International*.

Löer, K., Toledo, T., Norini, G., Zhang, X., Curtis, A., & Saenger, E. H. (2020). Imaging the deep structures of the Los Humeros geothermal field, Mexico, using three-component ambient noise beamforming. *Seismological Research Letters*.

Pankow, K. (2016). *FORGE nodal array 1 [Dataset].* International Federation of Digital Seismograph. doi: 10.7914/SN/8J_2016

Picozzi, M., Parolai, S., & Richwalski, S. M. (2005). Joint inversion of H/V ratios and dispersion curves from seismic noise: Estimating the S-wave velocity of bedrock. *Geophysical Research Letters*, *32*(11), 1–4. doi: 10.1029/2005GL022878

Podgorney, R. (2020). *Utah FORGE: Earth Model Mesh Data for Selected Surfaces.* Retrieved from `https://gdr.openei.org/submissions/1107`

Saenger, E. H., Gold, N., & Shapiro, S. A. (2000). Modeling the propagation of elastic waves using a modified finite-difference grid. *Wave Motion*, *31*(1), 77–92. doi: 10.1016/S0165-2125(99)00023-2

Scherbaum, F., Hinzen, K. G., & Ohrnberger, M. (2003). Determination of shallow shear wave velocity profiles in the cologne, Germany area using ambient vibrations. *Geophysical Journal International*, *152*(3), 597–612. doi: 10.1046/j.1365-246X.2003.01856.x

Toledo, T. (2020). Local Earthquake tomography of the Los Humeros geothermal field. *in preparation*.

Tuan, T. T., Scherbaum, F., & Malischewsky, P. G. (2011). On the relationship of peaks and troughs of the ellipticity (H/V) of Rayleigh waves and the transmission response of single layer over half-space models. *Geophysical Journal International*, *184*(2), 793–800. doi: 10.1111/j.1365-246X.2010.04863.x

Wathelet, M., Jongmans, D., Ohrnberger, M., & Bonnefoy-Claudet, S. (2008). Array performances for ambient vibrations on a shallow structure and consequences over Vs inversion. *Journal of Seismology*, *12*(1), 1–19. doi: 10.1007/s10950-007-9067-x

Wells, D., Lin, F., Pankow, K., Baker, B., & Bartley, J. (2022). Combining Dense Seismic Arrays and Broadband Data to Image the Subsurface Velocity Structure in Geothermally Active South-Central Utah. *Journal of Geophysical Research: Solid Earth*, 1–42. doi: 10.1029/2022jb024070

Zhang, W., & Gao, J. (2021). Model parameterizations in the time-domain multi-parameter acoustic least-squares reverse time migration. *Acta Geophysica*(0123456789). doi: 10.1007/s11600-021-00540-6